Theses and Dissertations

May 2014

Surface X-Ray Diffraction Study on Polar Oxide Surface and Interface

Wei Han
University of Wisconsin-Milwaukee

Surface x-ray diffraction study on polar oxide surface and interface

by

Wei Han

A Dissertation Submitted in

Partial Fulfillment of the

Requirements for the Degree of

Doctor of Philosophy

in

Physics

at

The University of Wisconsin–Milwaukee

May 2014

ABSTRACT

SURFACE X-RAY DIFFRACTION STUDY ON POLAR OXIDE SURFACE AND INTERFACE

by

Wei Han

The University of Wisconsin–Milwaukee, 2014
Under the Supervision of Professor Paul Lyman

An atomic scale study of surface/interface structure is required to properly understand physical and chemical phenomena such as crystal growth, lubrication and electrochemistry. The stability of polar oxide surface has long been an interesting question. A bulk-terminated polar oxide surface comprises alternating layers of opposite charges, thus resulting in diverging surface energies. In order to reduce the surface energy, various reconstruction-stabilized MgO (111) surfaces have been reported experimentally. However, the atomic structure of the MgO $(111)\sqrt{3}\times\sqrt{3}R30^o$ reconstructed surface remains unclear. Using a third-generation X-ray source is one of the feasible methodologies to probe such a system due to its increase of sensitivity on the interface layer. Surface X-ray diffraction (SXRD) experiments were performed for the MgO$(111)\sqrt{3}\times\sqrt{3}R30^o$ reconstructed surface at Advanced Photon Source, Argonne National Laboratory. The sample surface was prepared at home laboratory by annealing in a tube furnace for 36hrs at 1050^0C, with N_2 flowing at rate 1 to 2 scft. Crystal truncation rod (CTR) and super structure rod (SSR) measurements were acquired in both the absence and presence of a thin layer of water, obtained by compressing the bulk water layer with a thin Kapton sheet. A differential evolution algorithm, GenX, was used to search for the appropriate atomic model of reconstructed structure. Some reasonable models are presented and discussed with quantitative calculation of optimizing parameters (R factor and

χ^2). Preliminary SXRD results of the dry surface and solid-liquid interface are compared. This determination will shed light on whether physical (as opposed to chemical) factors are operant in the formation of ice-like layers.

www.manaraa.com

TABLE OF CONTENTS

List of Figures

LIST OF TABLES

ACKNOWLEDGEMENTS

I would like to express my greatest appreciation to my advisor, Professor Paul Lyman. It was he who opened my horizons to the fantastic scientific world and taught me all the precious knowledge and methods. Without his support and encouragement I would not have accomplished this program.

Next thank all the staff at Argonne National Laboratory and Brookhaven National Laboratory for their selfless help. Special thanks to Dr Zhan Zhang, Dr Ross Harder and Dr Christian Schleputz.

Thank the professors in our department, especially the committee members: Professor Dilano Saldin, Professor Marija Gajdardziska-josifovska, Professor Michael Winert, and Professor Danial Agterberg. Thank them for putting in their time and hearts to help me accomplish all the tasks.

Thank all my colleagues on this research project. Sujatha, Kallol, Seth, Sara, Somendra, they made my learning experience full of joy and satisfaction. It was our friendship that lighten the darkness of difficulties.

Thank my dad and mom. Throughout my life, they always think I am the best child. I might not be the best student, but I am proud to be their daughter. It was them made me believe myself and never give up.

Many of life's failures are people who did not realize how close they were to

success when they gave up.

Thomas A Edison

Chapter 1

Polar oxide introduction

1.1   Polar oxide

Polar oxide surfaces are formed on some faces of crystals that consist of alternating layers of oppositely charged ions. The charges arranged parallel to these surfaces produce an accumulating dipole moment perpendicular to the surface. This results in a high surface energy, which is of electrostatic origin. The polar compensation may be achieved either by a deep modification of the surface electronic structure, total or partial filling of surface states, sometimes leading to surface metallization by strong changes in the surface stoichiometry spontaneous desorption of atoms, faceting, large-cell reconstructions due to the ordering of surface vacancies,etc. [1] The atoms on the surface often rearrange in new configurations making the symmetry of the resulting surface different from the bulk. Surface structural problems fall into four broad categories: clean surface relaxations and reconstructions, adsorption site determinations, adsorbate-induced reconstructions, and interfaces. [2]

Polar oxide surfaces are subject to complex stabilization processes which result in interesting physical and chemical properties. Oxide surfaces have applications in many fields of research, which include geology, catalysis, electrochemistry, electronics, magnetic recording, and solid-state physics. They play a fundamental role in corrosion, friction, lubrication, etc.

On insulating oxides, surface oxygen atoms are more basic and surface cations are more acid than their bulk counter parts, generally resulting in a enhancement of the overall reactivity. On the other hand, reconstructed surfaces with large unit

cells may drive specific growth modes, favoring, for example, the formation of size-controlled clusters. In this point of view, polar surfaces of compound materials are of prominent interest. Moreover polar surfaces of compound semiconductors have been investigated intensively in the past. This is mainly due to the fact that the (100) surface of zinc-blende compounds serves as a substrate for the growth of nearly all III-V and II-VI device layers. This makes them the most important surfaces in semiconductor technology. [3]

Polar oxide surfaces present a vast number of diverse crystallographic structures-rock-salt, corundum, wurtzite, perovskite, etc. In addition, mixed-valence compounds, such as magnetite Fe_3O_4, can form when metal atoms with several oxidation states are involved, which allows one to stabilize oxides of different stoichiometries by playing with experimental parameters, such as temperature and partial oxygen pressure. [3]

Most of the usual techniques of surface science have been applied to investigate the atomic and electronic structure of polar surfaces of insulating materials. However, a complete characterization of the surface structure and stoichiometry is lacking for most of the systems considered so far. It is indeed difficult to conduct studies on insulators in general with charged particles. Moreover, to make quantitative LEED (low energy electron diffraction) analyses is still a challenge. Surface X-ray diffraction (SXRD) is a powerful technique to probe reconstructed surface structures. Since the volume of the surface region as compared that of the bulk is very low, the resulting scattered intensity from the surface is very weak. With the advent of brilliant synchrotron sources with very high intensity x-rays, SXRD has become a major technique in surface structure determination. Moreover it may easily be applied to insulating surfaces.

1.2   MgO(111)-the rock salt oxide

The rock-salt structure consists of two interpenetrating fcc lattices of anions and
cations. This structure is one of the most stable ones for highly ionic solids. The
MgO(111) surface is a typical example. The polar orientation is (111), the two-
dimensional unit cell is hexagonal, and the surface atoms are threefold coordinated.
(Figure 1.1)
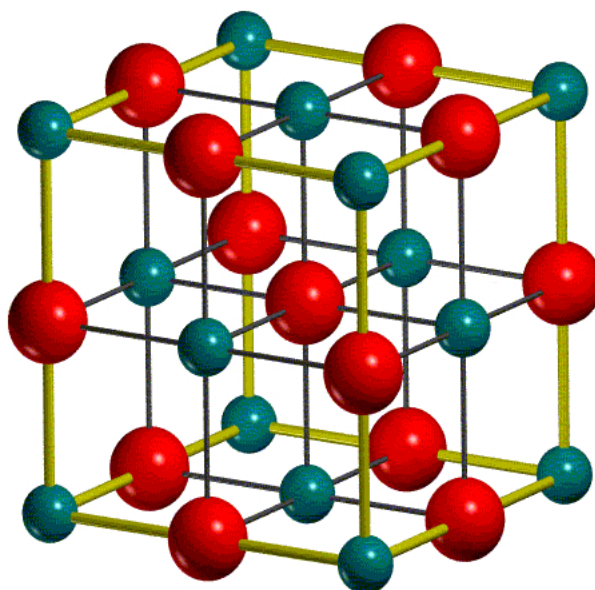
Figure 1.1: rock salt crystal [reference: www.theochem.unito.it/crystal_tuto/mssc2008_cd/
tutorials/geometry/geom_tut.html]

The MgO(111) surface has attracted a great interest because of its growing tech-
nological application and novel chemical activity. [4] [5] Early attempts to produce
(111) surface by truncation of bulk MgO led to non-planar surfaces, as evidenced
by LEED and scanning electron microscopy (SEM). [6] They were interpreted as
001 facets. But Plass *et al* have pointed out that they are actually {111} facets
resulting from acid etching in the sample preparation. [7] Three air-stable recon-
structions have been observed by transmission electron diffraction, on MgO (111)
samples annealed above 1450 ^{o}C, namely $(\sqrt{3}\times\sqrt{3})$ R30^o, (2×2), and $(2\sqrt{3}\times2\sqrt{3})$
R30^o. [8] Theoretical studies also proposed $(\sqrt{3}\times\sqrt{3})$ R30^o, (2×2), (2×1), and

$(2\sqrt{3} \times 2\sqrt{3})$ R30^o reconstruction on MgO(111) [9] [10] [7] Plass *etal* has reported cyclic ozone molecules bonded to the MgO surface, based on a transmission electron diffraction (TED). However the vertical spacing of the cyclic ozone over the second Mg layer can not be determined from two-dimensional TED data. TED combined with direct methods have been used by A. Subramanian and L.D. Marks [11]. It is suggested that $(\sqrt{3} \times \sqrt{3})$ R30^o reconstruction structure has vacancies in the top Mg layers, however, none of these models are consistent with the SXRD experimental data we have acquired. In this dissertation, the SXRD measurements are presented and some reasonable atomic structure models are discussed. Most of the fitting process was done using a genetic algorithm- GenX, which will be described in the later chapters. Results of different fitting parameters and outcomes are compared.

1.3 The ZnO (0001) and (000$\bar{1}$) wurtzite surfaces

ZnO can crystallize in the hexagonal wurtzite structure, in which each zinc (oxygen) atom is located at the center of an oxygen (zinc) distorted tetrahedron. ZnO is at the borderline between semiconductors and insulators. When cut along the polar (0001) or (000$\bar{1}$) directions, the crystal exhibits a Zn/O/Zn stacking of the hexagonal type AbBaA (capital letters for the Zn atoms, lower are for the O atoms), and the surface is Zn terminated or O terminated, respectively. The outer layer may consist of either A(a) or B(b) planes, which are rotated by 180° with respect to one another. The surface atoms are threefold coordinated. (Figure 1.2)

The (0001) and (000$\bar{1}$) surface of single-crystal ZnO are unreconstructed or reconstructed depending upon the surface preparation conditions. In particular, both cleaved and polished surfaces subjected to ion bombardment below 600°C exhibit a p(1×1) LEED diagram. Annealing at higher temperature may lead to (2×2), $(\sqrt{3} \times \sqrt{3})$, or $(4\sqrt{3} \times 4\sqrt{3})$ reconstructions, some of them being possibly due to surface contamination [12] [13] [14] [15] [16] [17] The diffraction patterns of the un-
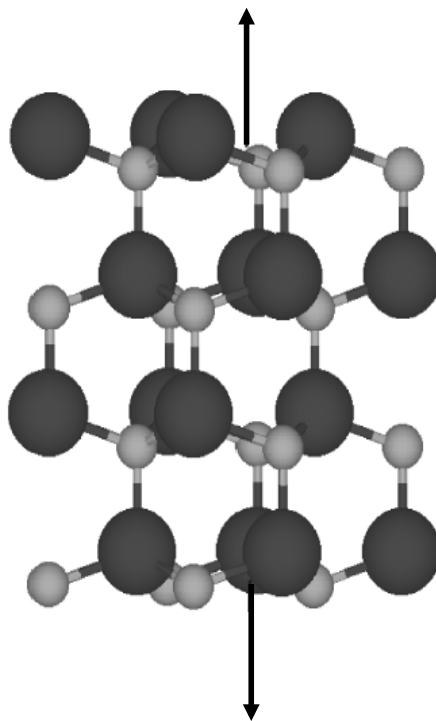
Figure 1.2: wurtzite crystal

reconstructed surface is expected to be sixfold rather than threefold symmetry from ideal bulk truncation. This was attributed to the presence of double steps on the surface [17], which were indeed detected in STM experiments, although no atomic resolution could be achieved [18] [19].

The atomic structure of the unreconstructed surfaces was quantitatively investigated by several techniques, including LEED [20], XPD [21], and GIXD [22]. It is reported in the GIXD study, for unreconstructed samples obtained after several cycles of Ar^+ bombardment and annealing at 800^oC, that the Zn surface presents a $+0.05$Å outward relaxation associated with a 0.75 occupancy of the Zn sites in the outer layer, as expected from electrostatic considerations. The O terminated surface is relaxed inward by -0.03Å , and the occupancies of both the outer and the underlying layers are different from those of the bulk. A density functional theory (DFT) calculation proposed a metallic surface. [23] Later works however suggested other stabilization mechanisms on the polar oxide surface. [24] [25]

Recently our group discovered a reconstruction on the $ZnO(000\bar{1})$ face that had not been seen in the earlier publications. LEED exhibits a clear $(\sqrt{3} \times \sqrt{3})R30^o$ pattern, which had only been observed on the Zn-terminated (0001) face before. [26] We conduct SXRD measurements on such novel surface, and features concluded from the experimental data are discussed.

Chapter 2

Experimental techniques

2.1   Ultra high Vacuum(UHV)

Ultra-high vacuum (UHV) is the vacuum regime characterized by pressures lower than about 10^{-7} Pa (10^{-9} mbar, or 10^{-9} torr). To acheive UHV pressures requires the use of special materials in construction and heating the entire system to, for example, 180°C for several hours ("baking"). The baking process is to remove water molecules and other trace gases adsorbed on the surfaces of the chamber.

Ultra-high vacuum is necessary for many surface analytic techniques such as: X-ray photoelectron spectroscopy (XPS), and Auger electron spectroscopy (AES), as well as thin-film growth and preparation techniques with stringent requirements for purity, such as molecular beam epitaxial (MBE), UHV chemical vapor deposition (CVD), and pulsed laser deposition (PLD). UHV is necessary for these applications for the following three reasons: to minimize collisions of particles with gases by increasing the mean free path, to control chemical and physical reactions by disturbing equilibrium conditions and to obtain clean surfaces by reducing the number of impacts of particles with surfaces.

To achieve ultra high vacuum requires specialized vacuum pumps Vacuum pumps can be broadly categorized according to three techniques. Positive displacement pumps mechanically expand a cavity, allowing gases to flow out from the chamber and be exhausted to the atmosphere. Oil sealed rotary, dry vane, and piston pumps are in this category. Momentum transfer pumps use high speed jets of dense fluid or high speed rotating blades to knock gas molecules out of the chamber; turbomolec-

ular, vapor diffusion and molecular drag pumps are examples. Entrapment- pumps capture gases in a solid or adsorbed state, and include cryopumps, getters, and ion pumps.

Diffusion pumps are the main vacuum generator in our home lab. They are operated with an oil of low vapor pressure. The attractive features of diffusion pumps are the high pumping speed for all gases and low cost per unit pumping speed compared with other types of pump with the same vacuum range. They can produce pressure down to 10^{-10}mbar, approaching 10^{-11}mbar with proper care. Although diffusion pumps cannot discharge directly into the atmosphere, a mechanical pump is usually attached to maintain a reduced outlet pressure (about 0.1 mbar).

Diffusion pumps are vapor jet pumps. The momentum transfer occurs when a heavy, high-speed vapor molecule collides with a gas molecule and moves it in a preferred direction through the pump. The bottom of the pump contains an electric heater, which is used to heat the pumping fluid to its boiling point thus producing the vapor. This must be done at a reduced pressure. This means that before the diffusion pump is started, the chamber must be lowered to an acceptable pressure by a mechanical pump as described above. Otherwise the multiple collisions with gas molecules will result in no pumping action and possible damage to the pumping fluid. Once the fluid begins to boil, the vapor is forced up the central columns of the jet assembly. It then exits at each downward directed jet in the form of a molecular curtain that collides with the pump body. The pump body is externally cooled so that the fluid will condense on its inside surface and run back down into the boiler. Pump bodies are typically water-cooled, but some are air-cooled. As gas molecules from the system randomly enter the pump, they encounter the top jet. Some of them are impacted and driven on to the next jet. Subsequently, they reach the foreline where they are exhausted to the atmosphere by the mechanical backing pump.[Figure 2.1]
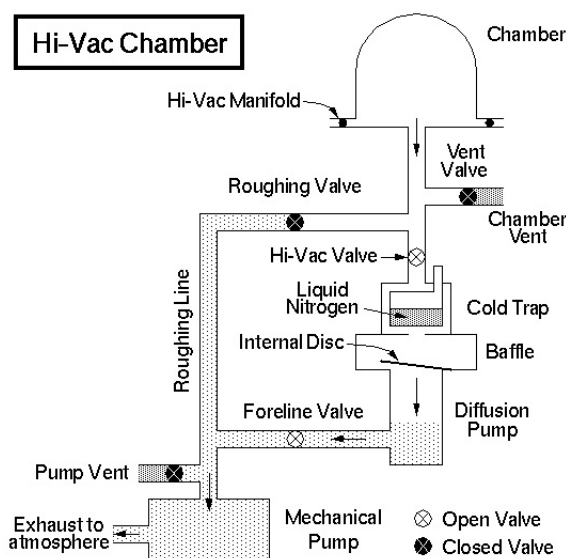
Figure 2.1: schematic drawing of a diffusion pump [reference: http://privatewww.essex.ac.uk / bolat /basicvacuumsystem.html)]

2.2 Low Energy Electron Diffraction (LEED)

The standard technique for the determination of surface symmetry, low energy electron diffraction (LEED), can be applied to reconstructed surfaces in a rather straightforward fashion. One short LEED measurement can give immediate and direct information about the surface order and quality. During the measurement, a collimated beam of low-energy electrons (30-300eV) is incident on sample surface and diffracted electrons are observed as spots on a fluorescent screen. When the surface is reconstructed or covered with adsorbates, the LEED patterns can quickly give some information about the surface symmetry and periodicities. LEED exploits the very strong interaction, both elastic and inelastic, of low energy electrons with atoms, which ensures the experiment is surface sensitive. Multiple scattering processes along with strong elastic scattering cross-section means structure determination has traditionally only been achieved by comparing the measured LEED intensities with the results of theoretical simulations for a series of trial structures, although a handful of structures have been determined though direct methods. [27] LEED intensities are typically more sensitive to displacements of atomic positions

perpendicular to the surface than parallel to it. [2]

In order to keep the sample clean and free from unwanted adsorbates, LEED is performed in an ultra-high-vacuum (UHV) environment (10^{-8}-10^{-10}mbar). After being mounted in the UHV chamber, the surface is cleared of weakly absorbed molecules by annealing at $550 - 600^oC$ for about 30 minutes. Sometimes 30 min of Ar^+ sputtering is needed to remove surface contaminants. The most important element in an LEED system is The electron gun and a display system.

In the electron gun, electrons are emitted by a cathode filament which is held at a negative potential, typically $10-600V$, with respect to the sample. The electrons are accelerated, focused into a beam and incident on the sample surface. Diffraction can be detected if sufficient order exists on the surface. This typically requires a region of single crystal surface as wide as the electron beam. A LEED detector usually contains three or four hemispherical concentric grids and a phosphor screen or other position-sensitive detector. The grids are used for screening out the inelastically scattered electrons.

The condition for the occurrence of an elastic Bragg spot is that the component of scattering vector parallel to the surface must equal a vector of the 2D surface reciprocal lattice, as described in following equations. [28]

$$\bar{K} \cdot \bar{a} = 2\pi h, \ \bar{K} \cdot \bar{b} = 2\pi k; \quad (h, k \ integer). \tag{2.1}$$

With

$$\bar{K} = \bar{K}_\parallel + \bar{K}_{perp}\hat{e}, \tag{2.2}$$

Equation (2.2) is fulfilled when

$$\bar{K}_\parallel = \bar{G}_\parallel. \tag{2.3}$$

This is called Laue condition.

Figure 2.2 shows the Ewald construction for elastic scattering on a 2D surface

lattice. According to the experimental geometry the wave vector k_i of the primary beam is positioned with its end at the (0,0) reciprocal lattice point and a sphere is constructed around its starting point. As is seen from Figure 2.2, the condition is fulfilled for every point at which the sphere crosses a reciprocal lattice rod. The
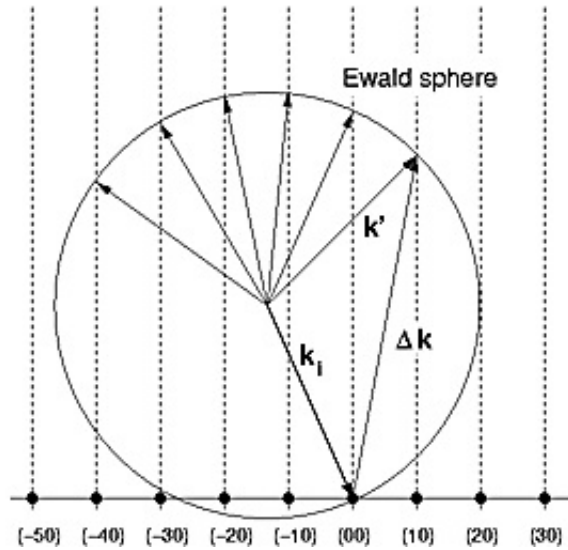
Figure 2.2: 2D Ewald construction for elastic scattering [http://www.fmc.uam.es/lasuam/glossary.php]

scattering condition for the plotted beams is fulfilled for the reciprocal lattice point $(hk)=(10)$, and a number of other reflections are also observed.

In a real LEED experiment, however, the primary electrons penetrate several atomic layers into the solid. The deeper they penetrate, the more that scattering in the direction normal to the surface contributes to the LEED intensities . The third Laue condition becomes more and more important. In the extreme case of 3D scattering, where the Laue conditions are exactly valid, the thicker regions of the rods become points of the 3D reciprocal lattice. When the Ewald sphere crosses a thicker region of the rods, the corresponding Bragg spot has strong intensity whereas less pronounced regions of the rods give rise to weaker spots. If we change the primary energy of the incoming electrons the magnitude of k, ie., the radius of the Ewald sphere, changes. As k is varied, the Ewald sphere passes successively
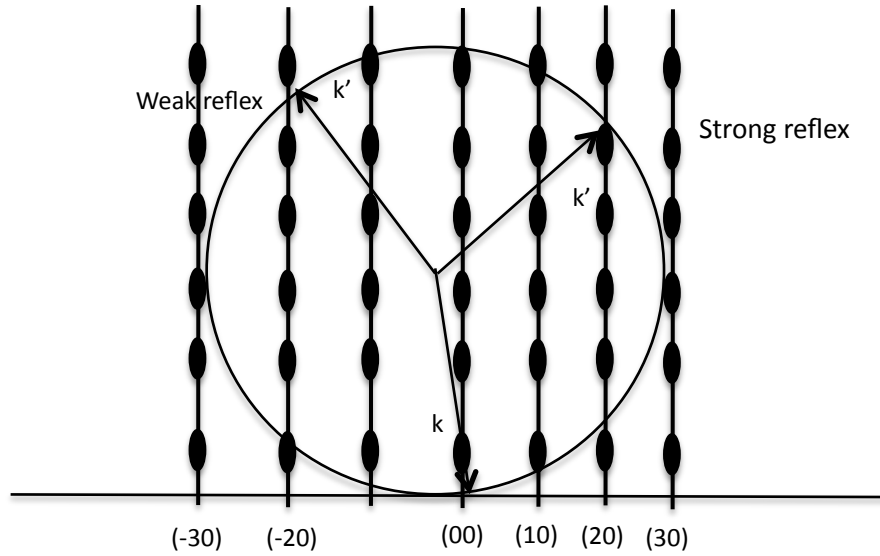
Figure 2.3: Ewald construction for elastic scattering on a quasi-2D surface lattice.

through stronger and weaker regions of the rods and the intensity of a particular Bragg spot varies periodically. In Figure 2.3, scattering not only from the topmost lattice plane but also from under-layers is taken into account. Correspondingly the $(2, 0)$ reflections has strong intensity whereas $(\bar{2}, 0)$ has weak intensity. [28]

2.3 Surface X-ray Diffraction (SXRD)

In contrast to LEED, surface X-ray diffraction (SXRD) exploits the weak elastic scattering of X-rays by atoms. X-rays penetrate deeply in matter, enabling the study of buried interfaces. In an X-ray diffraction measurement, a beam of X-rays strikes a crystal and diffracts into many specific directions. From the angles and intensities of these diffracted beams, one can produce a three-dimensional picture of the electron density, from which the mean positions of the atoms in the crystal can be determined, as well as their chemical bonds, their disorder and various other information.

Grazing incidence X-ray diffraction (GIXD) is a powerful technique to characterize single-crystal oxide surfaces and metal oxide interfaces. It is especially suited to investigate the structure and morphology of oxide surfaces, because it is not subject to charge build-up due to the insulating character of the surface. With the brightness of synchrotron radiation sources, one can measure diffraction from less than one monolayer of material. The grazing incidence geometry can drastically reduce the X-ray penetration in matter, down to 25 Å, and also reduce the unwanted bulk elastic and inelastic scattering with respect to the measured surface or interface elastic scattering. Surface sensitivity can be achieved by measuring diffraction rods that are specific to reflections arising from a surface reconstruction. [29]

One of the main applications of surface X-ray diffraction is study of semi-conductor surfaces, both the intrinsic reconstructions of clean surfaces and the adsorbate-induced structures. The motivation is to gain an understanding of the formation of semiconductor-metal and semiconductor-semiconductor (heterojunction) interfaces. One feature of semiconductor surface structures is that they can be complex with large surface unit nets, such as the intrinsic clean surface, Si(111) (7×7) structure. [30] In combination with Fourier transform methods, much success has been achieved solving surface reconstructions. These include the InSb(111)A (2×2)structure [31] [32], and Cu(110)(2×1) structure [33], [34] among many others.

2.3.1   Synchrotron Radiation

Synchrotron radiation light sources have continually evolved for more than fifty years. The first generation of synchrotron light sources were parasitic on machines designed as particle accelerators such as Synchrotron Ultraviolet Radiation Facility (SURF) at the National Bureau of Standards. The second generation of light sources were constructed as dedicated storage rings for synchrotron light production. It was not until the third generation that the machines were optimized for brightness.

Third generation synchrotron radiation light source provides X-ray with high brightness or flux per unit solid angle. The Advanced Photon Source (APS) is one such source, and is located at Argonne National Laboratory. In a synchrotron light source, charged particles travels at relativistic speeds in applied magnetic fields which force them to travel along curved paths. There are two ways of producing synchrotron radiation in a storage ring, bending magnets and insertion devices. The former keeps the electrons travel in a straight line within a closed orbit, and the latter, forces the electrons to follow oscillating paths. The insertion devices, known as wigglers or undulators, locate in the straight section of the storage ring. In wigglers, electrons travel in a series of circular arcs. The amplitude of the oscillations in a wiggler is large, thus produce incoherent sum of the radiation. Whereas in undulators, the amplitude of oscillations is rather small, therefore it is possible to construct the undulators such that the radiation at one oscillation is in phase with the next one. In this case, the radiation from each oscillation should add coherently. The main difference in the performance of these devices lies in the maximum angle of the electron oscillations in the horizontal plane. Undulator synchrotron radiation is highly collimated and well suited for diffraction measurements. [reference: $http : //xdb.lbl.gov/Section2/Sec_2 - 2.html$]

The quality of the X-ray beam produced from the synchrotron light source is characterized using a quantity called brilliance. It includes many aspects of an X-ray source and is defined as:

$$Brillian = \frac{Photons/second}{(mrad)^2(mm^2 sourcearea)(0.1\% bandwidth)} \qquad (2.4)$$

First, numbers of photons emitted per second need to be considered. Then it is the collimation of the beam, given in $mrad$, which is determined by how much the beam diverges as it propagates. Next the mm^2 source area defines the image size that the X-ray beam can focus to. Finally the issue of spectral distribution

A plan view of the APS facility showing (1) locations of x-ray beamlines and beamline operator groups, (2) scientific disciplines investigated at the APS, and (3) locations and arrangements of x-ray producing electromagnets and insertion devices in the electron storage ring.
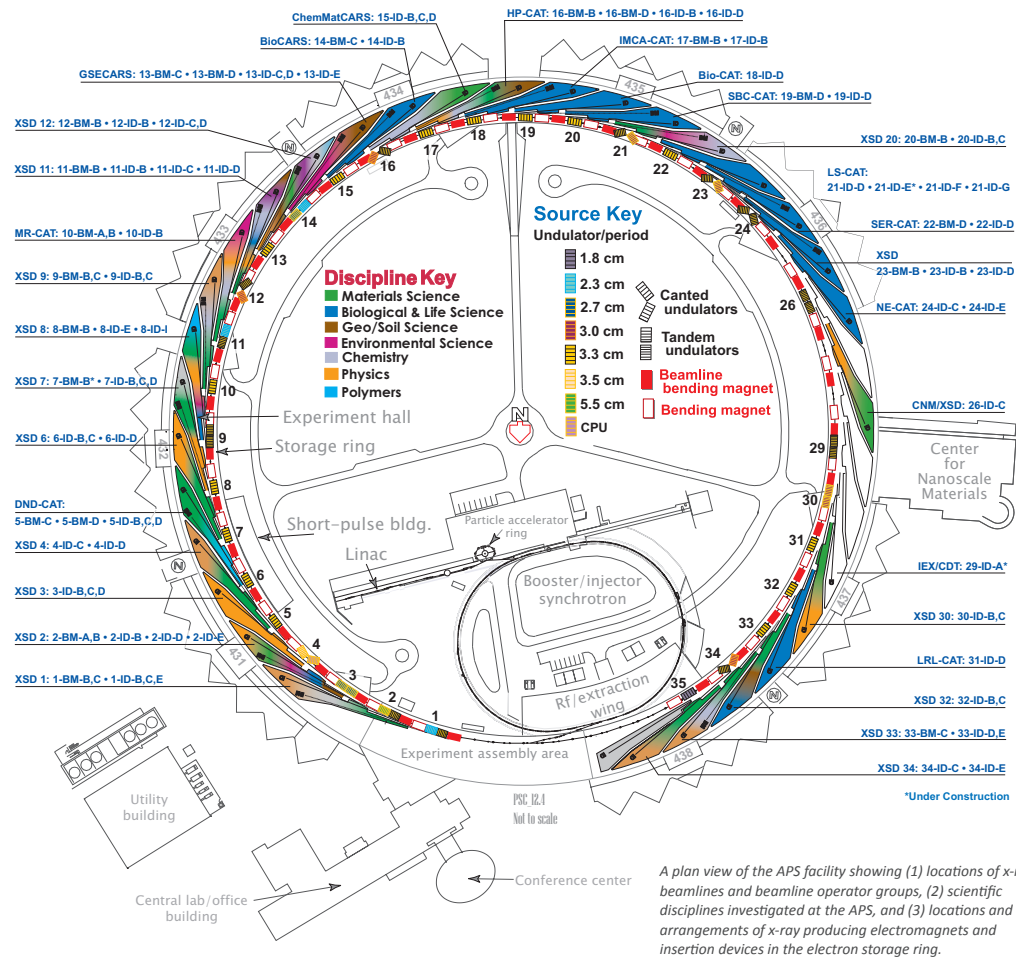
Figure 2.4: Synchrotron light source and various application using the radiation coming out tangential to the storage ring

is taken into account. The measured intensity is only a partial contribution from photon energies. Some spectra are smooth while some exhibit peaks at certain photon energies. The photon energy range is then defined with respect to energy bandwidth. To further reduce the spectral bandwidth of the radiation used for an experiment, a Bragg diffraction monochromator is used to select just a small range of wavelengths that satisfy the Bragg condition with a monochromator crystal. The intensity in photons per second after the monochromator is the product of the brilliance, angular divergences set by the horizontal and vertical apertures (in mili-radian), the source area(in mm^2), and the relative bandwidth of the monochromator

Bragg reflection relative to 0.1%. [35]

2.3.2 Diffractometer and detector

A diffractometer enables one to measure a large range of reciprocal space, thus allowing atomic coordinates to be determined with high accuracy in all three directions. A six-circle diffractometer was used in these X-ray diffraction experiments. This diffractometer has four degrees of freedom for the sample (ω, χ and ϕ and μ), and two for detector (δ, and ν) and a joint rotation. Such a diffractometer can be operated in many modes. The main mode used is grazing incidence mode, resulting good signal to noise ratio and surface sensitivity. In the symmetric mode, incident angle equals exit angle, is specifically used for reflectivity scan of the specular ($00l$) rod. The sample is mounted onto the goniometer, and carefully positioned at the center of all rotations. Lasers are used for alignment and the reflected laser beam from the sample helps to coordinate sample with the circular motors. An orientation matrix, which transforms the motor angles to the sample surface miller index system (hkl), is obtained by locating Bragg reflections from known information of the bulk structure. Experimental data are obtained as diffraction intensities in terms of photon counts with diffractometer motor angles. Experimental data is extracted into plots of integrated diffraction intensity versus varying out-of-plane coordinate l at different in-plane (hk) rods. Geometrical and resolution corrections are applied to account for instrumental errors. Once all correction factors are applied, it is straightforward to extract the structure factor, which is the quantity of interest in a crystallography experiment, from the integrated intensity. [36]

The Pilatus detector is a fast digital X-ray camera operated in single photon counting mode at. It consists of a 487×195 array of individual detectors. The main features include: no dark current background; no readout noise; an excellent point spread function; and short readout time. Different than traditional point detectors,

the Pilatus detector collects the entire diffraction reflection in a single measurement at given detector angles, since the unrestricted beam is allowed to flood the sample. Therefore, the full extent of the CTR signal where it intersects the Ewald sphere is recorded in a single image. Once reduced, we have a set of structure factor amplitudes at a large range of Miller indices of the reciprocal lattice. [37]
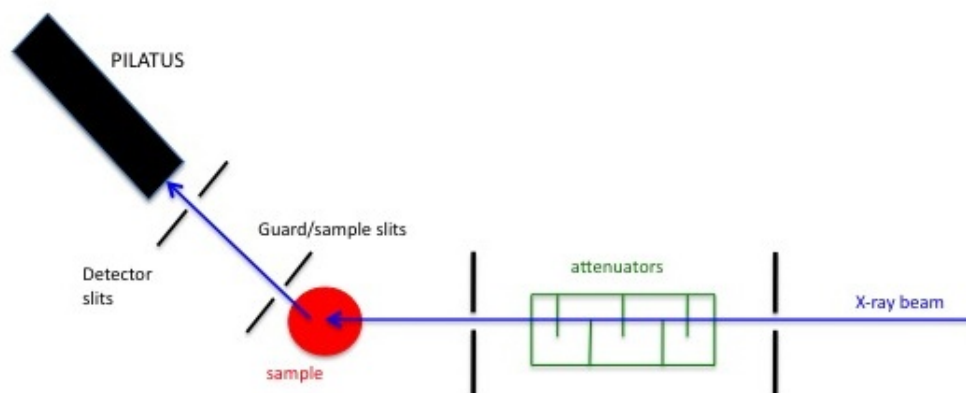
Figure 2.5: Experiment setup

The experiment setup is shown in Figure 2.5. The collimated and monochromatic x-ray beam comes from the beamline optics system. The first slit is to make sure of the collimation of the beam. The second slit is to control the footprint of the beam on the sample. The attenuators are a set of metal foils which attenuate the incoming X-ray beam, especially when close to a Bragg peak. It is carefully calibrated so the attenuation can be accurately calculated and accounted in diffracted intensity. The guard slits are mounted on the front of the detector arm. They are opened up enough to capture the entire diffraction signal from the sample and eliminate background signal arising from, e.g. Be dome, air scattering, etc.

Chapter 3

Theory background

3.1 Scattering from a crystal lattice

A crystalline material is characterized by the fact that it may be constructed by periodically repeating a basic structural unit, known as the unit cell. The points at which the unit cell are located form a lattice which may exist in one, two, or three dimensions. Thus a crystal is constructed by first specifying the lattice, and then associating a collection of atoms known as a basis with each point in the lattice.

A two-dimensional lattice is specified by a set of vectors R_n with

$$R_n = n_1 \bar{a}_1 + n_1 \bar{a}_2 \tag{3.1}$$

where $\bar{a}_1$ and $\bar{a}_2$ are the lattice vectors, and n_1 and n_2 are integers. The vectors $\bar{a}_1$ and $\bar{a}_2$ define the unit cell. It is important to note that the choice of lattice vectors is to a large extent arbitrary. A given specified lattice has characteristic symmetries. For example, the lattice shown in Figure 3.1 has a two fold rotation axis through the origin and perpendicular to the plane of the paper. This enables lattice to be classified into types, and in 1845 Bravais showed that in 2D there are 5 distinct types of lattice and in 3D there are 14. [35] On the other hand, for any lattice, we can choose the lattice vectors such that the area of the unit cell (or volume in three dimension) is a minimum. This is known as primitive unit cell, which contains just one single lattice point. The advantage of working with a primitive unit cell is it minimize any possible ambiguities and might be easier to visualize the structure.

To complete the description of a crystal structure we need to associate a basis
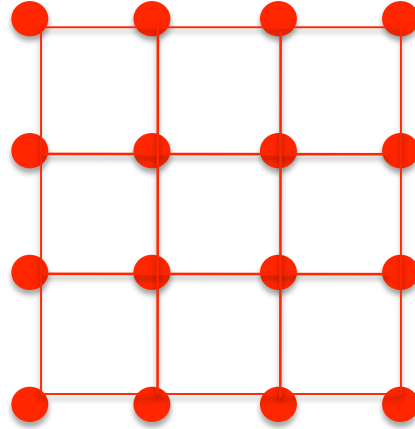
Figure 3.1: Lattice with two fold rotation symmetry

of atoms with every lattice site. When the possible symmetries of the basis are combined with those of the lattice it turns out that all crystal structures can be classified into one of 32 possible point groups and one of 230 possible symmetry groups, as described in standard books on crystallography. Lattices that exist in the real space occupied by the crystal are known as direct lattices to distinguish them from ones that may be defined in other spaces.

X-ray diffraction from a crystalline material is concerned with the scattering from atoms that lie within families of planes in the crystal, and it is necessary to have some way to specify a given family of planes. The Miller indices turn out to be the most convenient way to achieve this. For a given family of planes, the Miller indices(h, k, l) are defined such that the plane closest to the origin has intercepts $(a_1/h, a_2/k, a_3/l)$ on the axes (a_1, a_2, a_3). There are two important features of planes specified by their Miller indices. The first is that the density of lattice points in a given family of planes is the same, and that all lattice points are contained within each family. The second is that the planes are equally spaced, so that it is possible to define a lattice spacing d_{hkl}. For example, it may be shown that the d-spacing of a cubic lattice is given by

$$d_{hkl} = a/(\sqrt{h^2 + k^2 + l^2}),$$ (3.2)

where a is the lattice parameter.

3.2 The Laue condition and reciprocal lattice

We can now proceed to calculate the scattering amplitude. A given atom in the crystal may be thought of as belonging to a basis associated with a particular unit cell. The position of the atom in the crystal may then be written as $R_n + r_j$, where R_n specifies the origin of the unit cell and r_j is the position of the atom relative to that origin. The scattering amplitude for the crystal factorizes into two terms and it may be written as

$$F^{Crystal}(Q) = \sum_{r_j} F_j^{mol}(Q)e^{iQ\cdot r_j} \cdot \sum_{R_n} e^{iQ\cdot R_n}.$$ (3.3)

The first factor is the scattering amplitude from the basis of atoms contained within the unit cell and is known as the unit cell structure factor:

$$F^{Crystal}(Q) = \sum_{r_j} F_j^{mol}(Q)e^{iQ\cdot r_j},$$ (3.4)

where r_j is the position of the jth atom in the unit cell. The second factor is the sum of the unit cells in the lattice.

The number of terms in the lattice sum is enormous. Each of the terms is a complex number with phase, $e^{i\phi_n}$, located somewhere on the unit circle. The sum of phase factors is of order unity, except when all phases are 2π or a multiple thereof, in which case the sum will be equal to the huge number of terms. The problem is then to solve

$$Q \cdot R_n = 2\pi \times integer. \tag{3.5}$$

To find a solution, suppose that we now construct a lattice in the wavevector space (which has dimensions of reciprocal length) spanned by basis vectors (a_1^*, a_2^*, a_3^*) which fulfill

$$\bar{a}_i \cdot \bar{a}_j^* = 2\pi\delta_{ij}, \tag{3.6}$$

where δ_{ij} is the Kronecker delta, defined so that $\delta_{ij} = 1$ if $i = j$ and is zero otherwise. The points on this reciprocal lattice are specified by vectors of the type

$$\bar{G} = h\bar{a}_1^* + k\bar{a}_2^* + l\bar{a}_3^*, \tag{3.7}$$

where h, k, l are all integers. Now the reciprocal lattice vector satisfy Equation (4.2)since the scalar product of G and R_n is

$$\bar{G}.\bar{R}_n = 2\pi(hn_1 + kn_2 + ln_3), \tag{3.8}$$

and, as all of the variables in the parentheses are integers, the sum of their product is also an integer. In other words, only if $\bar{Q}$ coincides with a reciprocal lattice vector will the scattered amplitude from a crystallite be non-vanishing. This is the Laue condition for the observation of X-ray diffraction:

$$\bar{Q} = \bar{G} \tag{3.9}$$

The Laue condition is a vector equation, requiring that each component of the momentum transfer equals the corresponding component of the reciprocal lattice vector. Only when this condition is fulfilled will all of the phases of the scattered waves add up coherently to produce an intense signal. The Laue condition provides

a mathematically elegant, but powerful, way to visualize diffraction. In order to calculate intensities it is of course necessary to explicitly calculate the lattice sum.

One remaining problem is to find an algorithm to generate the basis vectors of the reciprocal lattice. In one dimension the construction of the reciprocal lattice is obvious. In two and three dimensions the situation is a little more complex, and it may be shown that the reciprocal lattice basis vectors are

$$\bar{a}_1^* = \frac{2\pi}{v_c}\bar{a}_2 \times \bar{a}_3; \ \ \bar{a}_2^* = \frac{2\pi}{v_c}\bar{a}_3 \times \bar{a}_1; \ \ \bar{a}_3^* = \frac{2\pi}{v_c}\bar{a}_1 \times \bar{a}_2 \tag{3.10}$$

where $v_c = \bar{a}_1 \cdot (\bar{a}_2 \times \bar{a}_3)$ is the volume of the unit cell.

In two dimensions $\bar{a}_3$ is chosen to be a vector normal to the 2D plane spanned by $\bar{a}_1$ and $\bar{a}_2$. For the 2D square lattice, the reciprocal lattice is also square with a lattice spacing of $2\pi/a$. If the axes are not orthogonal, as is the case for the 2D hexagonal lattice, then the basis vectors in real and reciprocal space are not necessary parallel. As an example in three dimension, the primitive basis vectors for the face centered cubic (fcc) lattice are

$$\bar{a}_1^* = \frac{4\pi}{a}(\frac{\hat{y}}{2} + \frac{\hat{z}}{2} - \frac{\hat{x}}{2}); \ \ \bar{a}_2^* = \frac{4\pi}{a}(\frac{\hat{z}}{2} + \frac{\hat{x}}{2} - \frac{\hat{y}}{2}); \ \ \bar{a}_3^* = \frac{4\pi}{a}(\frac{\hat{x}}{2} + \frac{\hat{y}}{2} - \frac{\hat{z}}{2}) \tag{3.11}$$

These are in fact the primitive basis vectors of a body centered cubic lattice with a cube edge of $4\pi/a$.

The Bragg equation

$$2d\sin\theta = m\lambda \tag{3.12}$$

can be derived from Laue equation making use of the relationship between points in reciprocal space and planes in the direct lattice. For each point of the reciprocal lattice given by Equation (3.7) there are a set of planes in the direct lattice satisfying the condition below:

1. G_{hkl} is perpendicular to the planes with Miller indices(h, k, l).

2. $|G_{hkl}| = 2\pi/d_{hkl}$, where d_{hkl} is the lattice spacing of the (h,k,l) planes.

Now the Laue condition $Q = k' - k = G$ can be written in the form, $k = G + k'$. Taking the square of both sides yields the result

$$k^2 \;=\; G^2 + 2Gk + k'^2 \tag{3.13}$$

$$|k| \;=\; |k'| \tag{3.14}$$

$$G^2 \;=\; 2G \cdot k \tag{3.15}$$

Equation 3.14 is based on the fact that the scattering is elastic. Considering if G is a reciprocal lattice vector, then so is -G. Therefore

$$G \cdot k \;=\; Gk \sin\theta \tag{3.16}$$

$$since \quad G \;=\; 2\pi/d \tag{3.17}$$

Equation (3.16) can be written as

$$\lambda = 2d \sin\theta \tag{3.18}$$

Thus it is proven the equivalence of Laue's condition and Bragg's equation. [35]

3.3 Scattering Theory

3.3.1 Scattering from a single electron

The wavelength of X-rays is comparable with the interatomic spacing. The Thompson formula (warren 1969) describes the amplitude of the wave A_1 that scattered from a electron situated at r_e, is given by,

$$A_e e^{-ik_f.r_e} = A_0 \frac{e^2}{mc^2}.\frac{1}{R_0}.e^{-ik_i.r_e} \tag{3.19}$$

where A_0 is the amplitude of the wave goes in to the electron; e and m are electron charge and mass, R_0 is the distance to the observer. $\frac{1}{R_0}$ arises because a spherical wave comes out when a plane wave goes in.

With a small charge of electron and large value of speed of light the constant $\frac{e^2}{mc^2}$ is very small, meaning, the total scattering cross section from even a large number of electrons is still quite small. Therefore, the kinematical approximation is valid, in which the amplitude scattered by an object is taken to be the sum of independent contributions from all individual electrons.

The theoretical scattering amplitude can be derived below:

$$A_e = A_0 \frac{e^2}{mc^2} . \frac{1}{R_0} . e^{-ik.r} . e^{(k'r)} = A_0 \frac{e^2}{mc^2} . \frac{1}{R_0} . e^{-i(k'-k)r} = A_0 \frac{e^2}{mc^2} . \frac{1}{R_0} . e^{-iq.r}, \qquad (3.20)$$

where the momentum transfer is related both to the experimental scattering angle, 2θ. The results of a scattering experiment may be thought of as a map in momentum space, where the scattered intensity is a function of q.

3.3.2 Scattering from a charge distribution

In summation of the scattering amplitudes from each electron in an atom, it is necessary to consider electron density distributions. When considering a distribution of charges rather than a single point charge, the scattered wave is summed up from contributions of the secondary waves emitted from each scattering center. For N individual scatters at position r_j The total amplitude A_{charge} is calculated through the coherent addition of all individual waves.

$$A_{charge} = A_0 \frac{e^2}{mc^2} . \frac{1}{R_0} \sum_{j=1}^{N} e^{iq(R_n + r_j)} = A_0 \frac{e^2}{mc^2} . \frac{1}{R_0} e^{iqR_n} \sum_{j=1}^{N} e^{iqr_j} \qquad (3.21)$$

This summation then becomes a integration:

$$A_2 = A_0 \frac{e^2}{mc^2} \frac{1}{R_0} \int \rho(r') exp(iq \cdot (R_n + r_j + r')) d^3 r' \tag{3.22}$$

$$= A_0 \frac{e^2}{mc^2} \frac{1}{R_0} f(q) exp(iq \cdot (R_n + r_j)) \tag{3.23}$$

where $\rho(r')$ is charge density from a continuous charge distribution.

3.3.3 Scattering from an atom

From last equation, we have

$$f(q) = \int \rho(r') e^{(iq \cdot r') d^3 r'}. \tag{3.24}$$

$f(q)$ is called the atomic form factor. It is the Fourier transform of the electron density for a single atom. The atomic form factor is written as a function of the magnitude of the momentum transfer, independent of direction, because in almost all cases the atom is spherically symmetric. If examine one extreme case,

$$f(q = 0) = \int \rho(r') d^3 r' = Z, \tag{3.25}$$

it could help us to understand that $f(q)$ is strongly dependent of atomic numbers. More strictly speaking, it is somewhat energy dependent because the x-ray can excite atomic transitions. The values of f(q) are available in tabulated form in the "International Tables for Crystallography".

3.3.4 Scattering from the unit cell

The next step is to add up the atoms inside one unit cell of the crystal.

$$A_u c = A_0 \frac{e^2}{mc^2} \frac{1}{R_0} F(q) e^{(iq.Rn)} \tag{3.26}$$

Where

$$F(q) = \sum_{j=1}^{N_c} f_j(q)e^{(iq.r_j)}. \tag{3.27}$$

The function $F(q)$ which is the sum over all the atoms within one unit cell, and it can be called the structure factor. It contains all the information about the structure of that unit cell, that is both the positions of the atoms and also their type as given by the atomic form factor. The structure factor is essentially the Fourier transform of the electron density for one unit cell of the crystal.

3.3.5 Scattering from an ideal bulk crystal

Finally we arrange the unit cells to make a three dimensional crystal lattice. This is where the scattering becomes strongly focused into beams along certain directions and then called diffraction.

$$A_c = A_0 \frac{e^2}{mc^2} \frac{1}{R_0} F(q) \sum_{n=0}^{N_1-1} \sum_{n_2=0}^{N_2-1} \sum_{n=0}^{N_3-1} exp(iq \cdot R_n). \tag{3.28}$$

The diffracted amplitude can be written as a product of slit functions,

$$A_c = A_0 \frac{e^2}{mc^2} \frac{1}{R_0} F(q) S_{N_1}(q \cdot a_1) S_{N_2}(q \cdot a_2) S_{N_3}(q \cdot a_3). \tag{3.29}$$

$S_N(qa)$ is sharply peaked at $q = 2\pi m/a$ where m is an integer, and tends in the limit to a periodic array of delta functions with a spacing of $2\pi/a$. This tells us that the diffracted intensity from a crystal has the special property of being only along specific, well-defined directions.

3.3.6 Intensities from amplitudes

In a real experiment, one can not measure the complex amplitude of the scattered wave, but only the real-valued intensity I. It is the squared modulus of the amplitude

or the product of the amplitude with its complex conjugate:

$$I = |A|^2 = A \cdot A^* \tag{3.30}$$

So the measured intensity at a certain hkl point is given by

$$I_{hkl} = |A_0 \frac{e^2}{mc^2} \frac{1}{R_0} F(hb_1 + kb_2 + lb_3) N_1 N_2 N_3|^2. \tag{3.31}$$

b_1, b_2, b_3 are reciprocal lattice vectors. [38]

3.4   Crystal truncation rod (CTR) and surface structure rod (SSR)

For an infinite crystal, the diffracted pattern is concentrated in delta function like Bragg peaks. The presence of crystalline surfaces results in additional structure along so-called crystal truncation rods (CTR). Figure 3.2 presents real space surfaces and their corresponding diffraction patterns in reciprocal space. Considering Equation (3.29), if the normal to surface direction is $\bar{a}_3$, the isolated monolayer is treated as setting $N_3 = 1$. The diffraction is independent of $q \cdot a_3$ in this case, which is the component of momentum transfer perpendicular to surface. The diffraction will be an array of rods (Figure 3.2 (b)). These rods represent the key features of diffraction from a surface. If the surface contribution to Bragg diffraction is added to the total Bragg diffraction. The rods are no longer flat in their intensity profile but exhibit diffuse intensity between Bragg peaks. (Figure 3.2 (d)). This is where the term "crystal truncation rods" (CTRs) come from [30].

CTR are very sensitive to surface changes and adsorbates. Even just a rough bulk surface would have an influence on the CTR profile. [30]. Simulated CTR data, for a structure where just the topmost atomic layer is relaxed along the out-
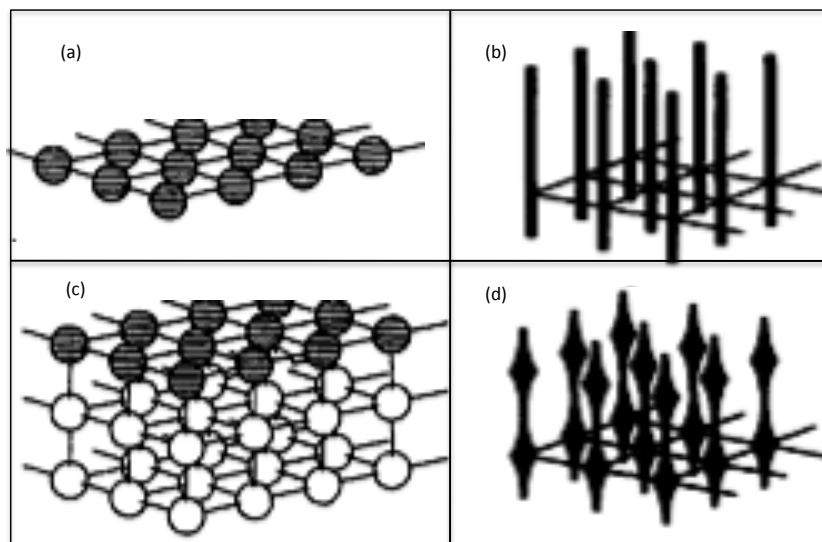
Figure 3.2: Schematic diffraction patterns corresponding to real space surfaces (a) real space isolated monolayer; (b) reciprocal space diffracted pattern of (a); (c) real space surface of crystal; (d) reciprocal space diffracted pattern of (c)[from Ian Robinson and Tweet [Rep. Prog. Phys, 55(5):599-651]]

of-plane direction by up to 10% of a unit cell spacing, exhibits dramatic changes in result. (Figure 3.3) The reason is between Bragg peaks, the contributions due to bulk atoms add destructively, and the small deviations away from the complete destructive interference will dominate the diffraction signal.

When a surface is reconstructed it will often show a different periodicity in the plane of surface. This different periodicity will give rise to so-called Surface
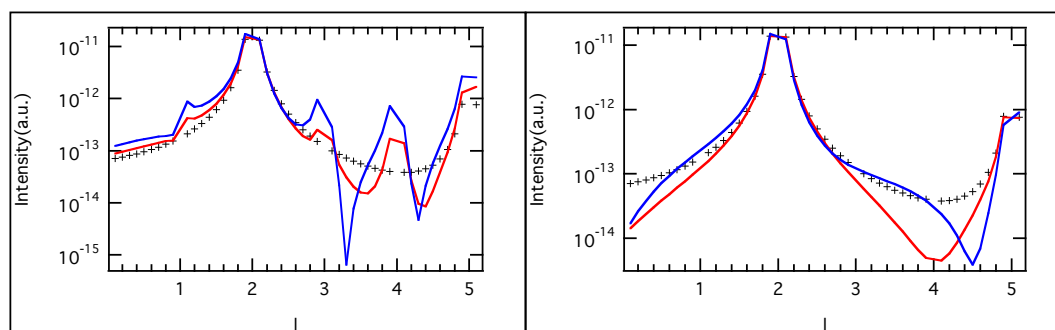
Figure 3.3: Simulation of CTRs demonstrating sensitivity of CTR to surface structure change. Left: topmost atomic layer is relaxed 10%(red) and 5%(blue); right: add one (red)/two (blue) atomic layers on surface

Structure, or Super structure rods (SSRs). Since there is no contribution to these rods from the bulk of the sample, they have strong sensitivity to the atomic structure of the surface unit cell. The periodicity in l also provides a way of determining the thickness of reconstructed surface layers.

3.5   Direct Method and PARADIGM

In surface crystallography, the main purpose is to determine the atomic structure of the surface layers as it is different from the known bulk. In the crystallography of bulk samples, the measured intensities of Bragg spots are proportional to the square of the amplitudes of Fourier components of the electron density of the unit cell. An approximation of that electron density can be found by an inverse Fourier transform if phases to each of these Fourier components can be estimated. Crystals usually have a small number of atoms per unit cell, and information loss caused by the missing phase can be compensated by iterative optimization methods which force the electron density to agree with the measured data as well as some physical conditions. These methods are called direct methods, and in bulk crystallography the physical conditions are usually that the electron density should be positive and atomic-like. There are two problems to recover directly the entire surface electron density : (1) to isolate the scattering contributions of the surface structure factors to the CTR intensities and (2) to determine the phases associated with the amplitudes of the SSRs.

This algorithm is based on previous algorithm by Miao et al. (1999). It can find phases associated with measured diffraction intensities, and also retrieve electron density from the diffracted amplitude, hence it is named phase and amplitude recovery and diffraction image generation method (PARADIGM) [39]

It was shown by Saldin *et al*. ([40] [40]) that the electron density of a surface may be recovered from SXRD data by a Fourier recycling method together with

information about the crystal structure of the bulk. Furthermore, such an algorithm was applied to the recovery of the surface electron density of clean Au (110) ([41]) and Sb-covered Au (110) [42] from experimental data.

The PARADIGM algorithm can be described as a set a repeated cycles between real space and reciprocal space. The cycles start from a flat distribution $\{u_j\}$ of the surface electron distribution. The Fourier transform of $\{u_j\}$, $\{S_q\} = FT\{u_j\}$ may be regarded as an estimate of the surface structure factors. After adding Sq to the corresponding structure factor B_q of the bulk, the arguments of the resultant complex numbers would be estimates of phases $\{\phi(q)\}$ of total structure factor Fq, whose amplitudes are constrained to be the experimental value $|F_q^{obs}|$ (up to a scaling factor).

A revised estimates of structure factors $\{Tq\}$ may be obtained by subtracting bulk structure factors from these estimates of the total structure factors.

$$T_q = C_n|F_q^{obs}|e^{i\phi q} - B_q. \tag{3.32}$$

An inverse Fourier transform of these quantities would give a new estimate of the surface electron density $\{t_j\} = FT^{-1}\{T_q\}$ that is constrained by the experimental data. The constraint of compact support is applied next: In the out-of-plane direction, the height of the surface slab can be estimated, which defines our region of compact support. This will give an estimate of the extent of the surface electron density in the direction of a_3, which will be about twice the height of the surface slab. Since the diffraction rods was sampled at quite fine intervals along the rods, a Fourier transform of such data used to calculate $\{t_j\}$ will generally (especially when phases are not correct) give non-zero values over a larger range of heights than the real physical height of the surface electron density. A real space constraint may be

imposed to define a new estimate $\{u_j\}$ of the electron density.

$$u_j = t_j, \; j \; outside \; of \; \gamma \tag{3.33}$$

$$u_j = 0, \; j \; inside \; of \; \gamma \tag{3.34}$$

where γ is the region where electron density is not expected. The iteration continues until clear electron densities are retrieved.

3.6 Partial Patterson function

The three-dimentional Partial Patterson (pair correlation) function [43] [44] is given:

$$P(\mu, \nu, \omega) = \sum_{hkl} |F_{hkl}|^2 cos[2\pi(h\mu + k\nu) + l\omega] \tag{3.35}$$

where μ and ν are fractional coordinates which span the unit cell. Equation(3.35) is true when all Fourier components are present, but the features of $P(\mu, \nu, \omega)$ becomes broadened when a truncated Fourier series is used. Patterson peaks separated by distances smaller than this resolution limit cannot be distinguished. $P(\mu, \nu, \omega)$ is usually represented as a contour map drawn on the real-space unit cell. It has the symmetry of the surface structure, provided all equivalents of the $F'_{hkl}s$ have been included, plus an additional centre of symmetry. It is usual to consider only the asymmetric repeating unit, which is some fraction of the full unit cell, as this contains all the information. [38]

A positive peak in $P(\mu, \nu, \omega)$ at (μ_0, ν_0, ω_0) means that two or more atoms in the structure are separated by the vector (μ_0, ν_0, ω). In general, however, an n-atom structure has $\frac{1}{2}n(n-1)$ independent vectors in the Patterson, and it may not be possible to interpret these in practice. Iterative procedures may then be used to find atoms one at a time, or else to search for known components of a structure

systematically.

3.7   ROD

Rod is a refinement program of surface structure using surface X-ray diffraction data. [45] ROD calculates structure factor F_{hkl} and optimize the structural model according to experimental measurements.

$$F_{hkl} = \sum_j f_j e^{-B_j Q^2/(16\pi^2)} e^{2\pi i(hx_j + ky_j + kz_j)}, \tag{3.36}$$

where f_j the atomic scattering factor of atom j, B the Debye-Waller parameter, (hkl) the diffraction indices and $(xyz)_j$ the position of atom j in fractional coordinates with respect to a unit cell.

For calculation of bulk structure factor, the summation will go over all atoms in the bulk unit cell. For surface X-ray diffraction we have to consider two separate parts: atoms belong to the surface and atoms in the bulk. The total structure factor of a surface diffraction is then given by the interference sum of both contributions:

$$F_{sum} = F_{surf} + F_{bulk}, \tag{3.37}$$

where

$$F_{surf} \quad = \quad \sum_j^{surface unit cell} f_j \theta_j e^{-B_j Q^2/(16\pi^2)} e^{2\pi i(hx_j + ky_j + kz_j)} \tag{3.38}$$

$$F_{bulk} \quad = \quad \sum_{j=-\infty}^{0} F_u e^{2\pi i l j} e^{j\alpha} \tag{3.39}$$

and

$$F_u = \sum_j^{bulk unit cell} f_j e^{-B_j Q^2/(16\pi^2)} e^{2\pi i(hx_j + ky_j + kz_j)} \tag{3.40}$$

Most of the case, indices are expressed in the bulk unit cell frame so that for reflections from bulk lattice occur at integer indices and reflections from a reconstructed surface with occur at fractional indices. Bulk unit cell structure factors sums from the top layer to $-\infty$, and surface structure factors sum from top layer to the positive out-of-plane direction. At fractional-order positions the bulk contribution is zero and the total structure factor equals F_{surf}. It is important to give all the atoms in the bulk unit cell the proper in plane coordinates, because only then will the bulk contribution cancel for 'fractional- order' reflections.

Symmetry-related domains might be taken into consideration for some simulations. It can be defined in programming whether to add domains coherently or incoherently. For convenience concern, rather than adding a additional unit cell to the computation, to add the structure factor for the original unit cell, but compute for the corresponding, symmetry-related diffraction indices through a symmetry operation matrix will arrive the same result, as shown below.

Suppose the surface has N_d domains. The structure factor of the nth domain is given by

$$F_{n,H} = K \sum_j e^{2\pi i r_{n,j} \cdot H} \tag{3.41}$$

K is a factor related to atomic scattering factor and Debye-waller fator.

Assume matrix A_n transform the coordinates of the first unit cell into that of a domain n, then,

$$F_{n,H} = \sum_j e^{2\pi i A_n r_{1,j} H} \tag{3.42}$$

Since

$$A_n r_{1,j} \cdot H = r_{1,j} \cdot A^{-1} H = r_{1,j} H'_n, \tag{3.43}$$

with

$$H'_n = A_n^{-1} H \tag{3.44}$$

Therefore, it is not necessary to apply the transformation matrix on the real

space coordinates. Transforming on the diffraction indices will achieve the same structure factor. In the summation over all domains in calculating structure factor, we can thus use one unit cell, but calculate the corresponding H_n' for each domain.

When optimizing a surface structure, displacement parameters are set up to change the positions of the atoms. Due to symmetry constraints, when one atom is moved, often also other atoms need to be displaced in a symmetric fashion. So besides magnitude of the displacement, the directions of movements are also controlled by defined constants.

The refinement of a structure is based on the measured X-ray diffraction data set by using a χ^2 minimization.

$$\chi^2 = \frac{1}{N-1} \sum_i \left(\frac{I_{obs} - I_{cal}}{\sigma_i}\right)^2, \tag{3.45}$$

3.8   Genetic algorithm and GenX

3.8.1   Genetic algorithm

A genetic algorithm is a refinement algorithm which implements a class of optimization routines, inspired by biological natural selection evolution. It is an alternative to the traditional optimization algorithms that does not require derivatives or other auxiliary knowledge. A genetic algorithm starts with a population of individual solutions and the quality of a solution is evaluated by calculating a fitness function. The evolution process is similar to "natural selection'and "survival of the fittest" get the better offspring by competition. This method was first introduced and investigated by John Holland at the University of Michgan in 1975. [46].

During the past decade, more and more genetic algorithms have been applied to solve the inverse problem in diffraction. One class of such algorithms has proven proven to be efficient and easily implemented, and is called differential evolution

(DE) algorithm [47] Storn & Price, 1997. The DE algorithm was first applied to diffraction and reflectivity data by Wormington et al.(1999) [48] and has been widely used. Examples include GenX ([49] Bjorck & Anderson, 2007), and Motofit([50] Nelson, 2006). DE has also been applied to powder diffraction ([51] Chong & Thremayne, 2006), the normal incidence X-ray standing wave technique ([52] Basham & Bennett, 2007), and surface X-ray diffraction ([53] [54]).

3.8.2   GenX algorithm- differential evolution

In GenX, the population of individuals in DE are defined by vectors $\{p_i\}$, which contains values for M parameters to be optimized. These parameter values are analogous to an individual's genes. The algorithm combines information from the parent population to form new members of the next population, a trial population, which will explore new points in the parameter search region.

The parent population, $P = \{p_0, p_1, \cdots, p_{N-1}\}$ and the trial population, $T = \{t_0, t_1, \cdots, t_{N-1}\}$ are of the same size. The trial population T is formed from the parent population P, starting with an initialization of random number parameters between their minimum and maximum values. The initialized population contains user-specified starting guesses from existing knowledge.

While trial population T is formed from the parent population P, mutation and recombination operators are applied. Each individual p_i serves as a parent for a trial individual t_i. Every generation, when the trial population is created, each individual is compared with its corresponding parent, meaning t_i is compared with p_i, through a fitness criterion, called the figure of merit (FOM). The individual with the lower FOM is selected to be a member of parent population of the next generation. Therefore only the improved population is allowed to propagate, others are eliminated. The iteration is repeated until the maximum number of generations have been reached or a manual criterion defined by the user has been satisfied.

The process that creates the trial population from the parent population is called the trial method. It is a combination of two different search strategies. One is mutation, which will search outside the current population and the other is recombination which is analogous to reproduction and combines the properties of different individuals.

The mutation process is done by a differential mutation operator, which represents the difference between two randomly selected parent individuals, indices r_1 and r_2. This difference is then scaled by a mutation constant k_m and added to a base vector, p_{base}, to form the mutated individual m;

$$m = p_{base} + k_m(p_{r1} - p_{r2}). \tag{3.46}$$

The maximum allowed movement away from the chosen base vector is determined by the spread in the population. The base vector p_{base} can be chosen at random or to be the best individual so far.

The recombination operation, combines the parameters in the current parent vector with the mutant vector. The probability that a mutant parameter will be inserted is given by the constant k_r. The final trial vector then becomes

$$t_{ij} = \begin{cases} m_{i,j} & \text{if rand} < k_r, \\ p_{i,j} & \text{otherwise} \end{cases} \tag{3.47}$$

When parameterizing a model for a diffraction measurement, it is easy to produce a model with strongly interdependent parameters owing to the underlying physical process of interference. One way of avoiding performance loss caused by interdependence is to use vector differences for the recombination as well, called arithmetic

line recombination. This can be expressed as

$$t_{ij} = p_{base} + \begin{cases} k_m(p_{r1} - p_{r2}) & \text{if rand} < p_f, \\ k_r(p_{r1} + p_{r2} - 2p_{base}) & \text{otherwise} \end{cases}. \tag{3.48}$$

where p_f is the probability for mutation only. The subscript "base" is the index of a random number. (Price et al., 2005)

Most real-world problems will need to implement some bounds on the parameters of the optimization problem, hence to avoid physically unreasonable values such as negative layer thicknesses or negative roughness values. It is also possible to restrict the search space to limit parameters within a physically reasonable interval.

3.8.3 Working with GenX

A data file consisting of h, k, l, intensity and intensity error is loaded through. A model to fit is defined in terms of python script which includes the following information.

1. A unit cell $(a, b, c, \alpha, \beta, \gamma)$ is created with all the parameters of the substrate. This also relates the (h, k, l) values in the measurement to the real world.

2. Both the bulk unit cell and surface are defined as slabs associated with each atom's position and chemical identity.

3. Symmetry operation is done by creating matrix operations and placing them in a list so we build up all allowed symmetry operations of the plane group.

4. All the above are combined to create a so-called sample prior to structure factor calculation.

5. A mandatory simulation function is defined which takes a data structure as input, loops though all loaded data sets, calculates the complex structure factor. Note that the intensity is the square of the absolute of the structure factor.

6. During each generation the figure of merit (commonly χ for X-ray diffraction)

is calculated, and movements of the atoms take place through variables dx, dy, dz for optimizing the fit between simulated data and measured data.

Chapter 4

Reconstructed MgO(111)

4.1 Introduction

In order to reduce the surface energy, various reconstruction-stabilized MgO (111) surfaces have been reported experimentally, namely $\sqrt{3} \times \sqrt{3}R30^o$, 2×2, and $2\sqrt{3} \times 2\sqrt{3}R30^o$. Most of the basic models of a (2×2) reconstruction is based on an octopole arrangement. [55] [56] However, the atomic structure of the MgO (111)$\sqrt{3} \times \sqrt{3}R30^o$ reconstructed surface remains unclear. The suggested MgO(111)$\sqrt{3} \times \sqrt{3}R30^o$ surface with vacancies in the top Mg layer does not agree with our experimental results. [11]

Using a third-generation X-ray source is one of the feasible methodologies to probe such a system due to its increase of sensitivity on the interface layer. Surface X-ray diffraction (SXRD) experiments were performed for the MgO (111)$\sqrt{3} \times \sqrt{3}R30^o$ reconstructed surface at the Advanced Photon Source, Argonne National Laboratory. Crystal truncation rod (CTR) and super structure rod (SSR) measurements were acquired.

A differential evolution algorithm, GenX, was used to search for the appropriate atomic model of the reconstructed structure. Some reasonable models are presented and discussed with quantitative calculation of optimizing parameters (R factor and χ^2).

4.2 Experiments

Double-sided polished MgO(111) 10×10 mm^2 single crystals (obtained from Crys-Tec Corporation) were placed between two MgO wafers. The sample stack, left in an alumina crucible, was loaded into a tube furnace and annealed at 1050^oC for 36 hours, with N_2 flowing at rate $1 \sim 2$ scfh. Afterward, the sample was mounted onto a Ta sample holder with "W"-shape clips, inserted into an ultra high vacuum (UHV) chamber for LEED and XPS analysis. Repeating in-situ ion sputtering was sometimes needed, followed by annealing to achieve order. The samples were removed from the vacuum chamber and transported to the synchrotron. SXRD experiments were conducted on the MgO(111)$\sqrt{(3)} \times \sqrt{(3)}R30^o$ reconstructed surface, enclosed in an evacuated beryllium dome. Crystal truncation rods (CTR) and superstructure rods (SSR) were acquired.

4.3 Results and analysis

4.3.1 Low energy electron diffraction (LEED)

As a qualitative first glance of the reconstructed surface, Figure4.1 shows the LEED pattern from a reconstructed MgO(111) surface. After a few sputter and anneal cycles, fractional order spots are evident within the (1×1) unit cell, corresponding to a $(\sqrt{3} \times \sqrt{3})R30^o$ reconstruction.

4.3.2 Atomic force microscope (AFM)

The morphology of the reconstructed surface is investigated by atomic force microscope (AFM). The surface seems quite smooth, the step size for most part of the sample is $+/-2nm$. Some triangular features appear on a reconstructed surface, which may reflect to the surface symmetry. After annealing in a UHV chamber, the
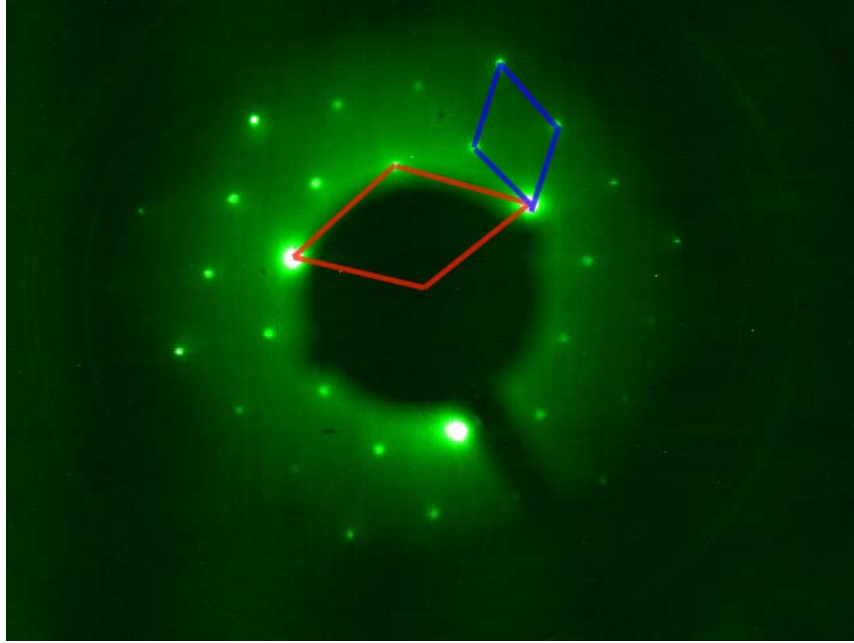
Figure 4.1: MgO(111)$\sqrt{(3)} \times \sqrt{(3)}R30^o$ reconstruction. Bulk(red) and superlattice(blue) unit cell are indicated

features are more distinct than before. (see Figure 4.2)

4.3.3 Surface X-ray Diffraction (SXRD)/ Grazing incidence X-ray diffraction(GXID)

Grazing incidence X-ray diffraction (GIXD) was used to study the surface. This technique is well suited to investigating metal-oxide interfaces since it is not hampered by the charge buildup. [29] [38] The experiments were conducted on the 34ID beamline at the Advanced Photon Source (APS), Argonne National Laboratory. Measurements were performed on a reconstructed single-crystal surface at $12.5 keV$ photon energy and at a systematical incidence angle of 0.1^o to reduce scattering from the bulk.

Lattice constants used as the input of experiments are $a = 2.978 \mathring{A}, b = 2.978 \mathring{A}, c = 7.295 \mathring{A}, \alpha = 90^o, \beta = 90^0, \gamma = 120^o$, which describes a MgO(111) 1×1 bulk lattice. The h and k indices are chosen to describe the in-plane momentum transfer in
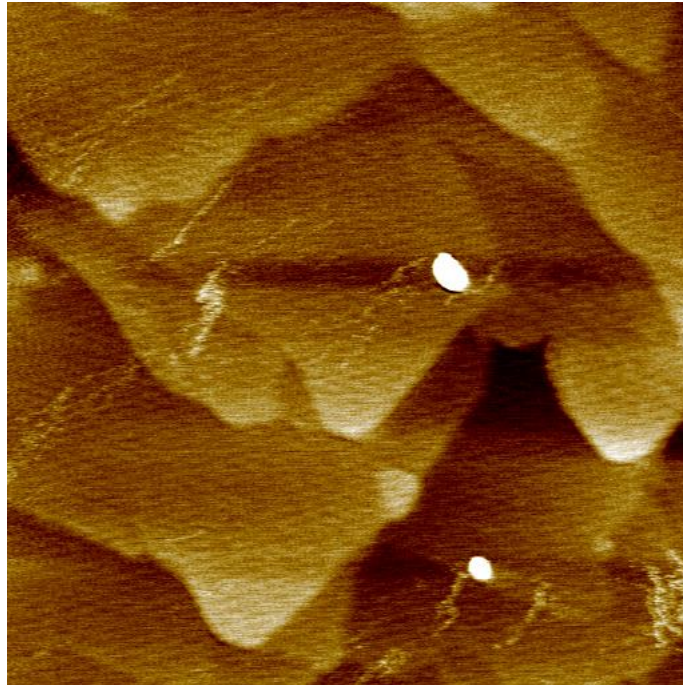
Figure 4.2: AFM image of a $(\sqrt{3} \times \sqrt{3})R30^o$ reconstructed surface
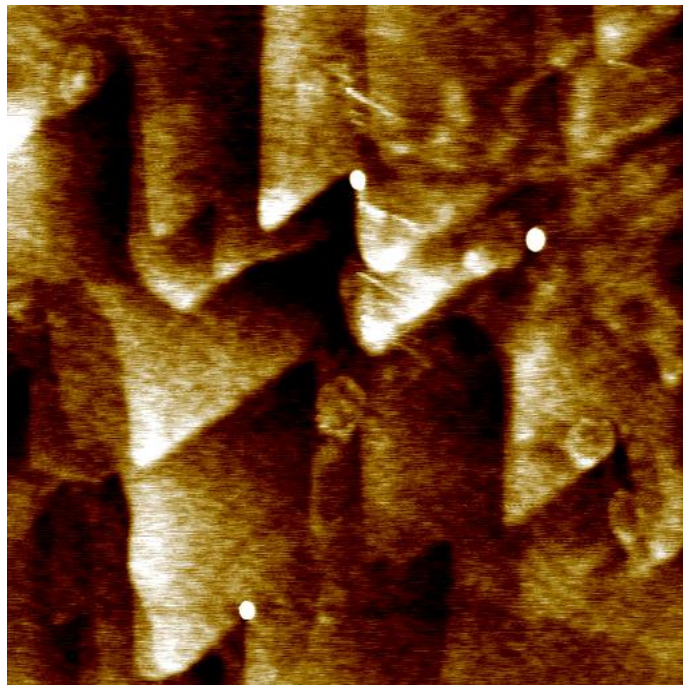
Figure 4.3: AFM image after aneal in a UHV chamber

reciprocal-lattice units of the MgO(111) reconstruction, and l for the perpendicular momentum transfer. In the reciprocal space, the angle between $(h00)$ and $(0k0)$ will be 60°, and $(00l)$ is still perpendicular to the surface.

For the quantitative measurements the opening of the two pairs of detection slits was set at $18mm$. A detailed data treatment is discussed below.

Data extraction

For using area detectors, the experimental integrated intensity is the area of the peak minus the background. A good approximation is to use the area under the histogram,

$$E_e = \sum_{i=1}^{N_s} S_i - \frac{N_s}{N_B} \sum_{i=1}^{N_s} B_i, \tag{4.1}$$

where S_i are the number of counts in each of the N_s bins of scan points, labeled signal, and B_i are the counts in the N_B background bins. E_e is in units of counts. The error in E_e due to counting statistics alone is

$$\sigma_E = \big[N_s \sum_{i=1}^{N_s} S_i + (\frac{N_s}{N_B})^2 \sum_{i=1}^{N_s} B_i \big]^{1/2}. \tag{4.2}$$

Extracting meaningful information from a raw detector image is the most critical and challenging step in the data analysis. Many factors including the shape, extent, positions, and orientation of a diffraction signal within the image may change considerably between different measurements on the same sample, and even within a single scan. The choice of window, outside which points are representative of background levels, can be conservative if the scans are wide enough. Possible sources of procedural error are cutting into the edge of the peak with the window or using too coarse a step size, both of which depress the value of E_e. Therefore, the main difficulty lies in the correct discrimination between the real signal and the background. Generally the background contains contributions from several different sources, such

as scattering from Beryllium windows or sample holders, a broad thermal diffuse scattering component from the sample itself, air scattering of the scattered beam, etc., and all the above may result in a complicated background distribution. On the other hand, the diffraction signals themselves may be smeared out due to crystal mosaicity of the sample, defect scattering, edge effects, a spatial inhomogeneity or large divergence in the incident beam intensity, possible sample curvature, etc.

The minimum criterion for a successful background discrimination is that the entire diffraction signal must be sharper than the smallest features in the background distribution. Only under these circumstances can one hope to predict with sufficient confidence what the background contribution within the signal should be. A region of interest containing the diffraction signal needs to be selected such that it encloses the signal as tightly as possible without cutting into it.
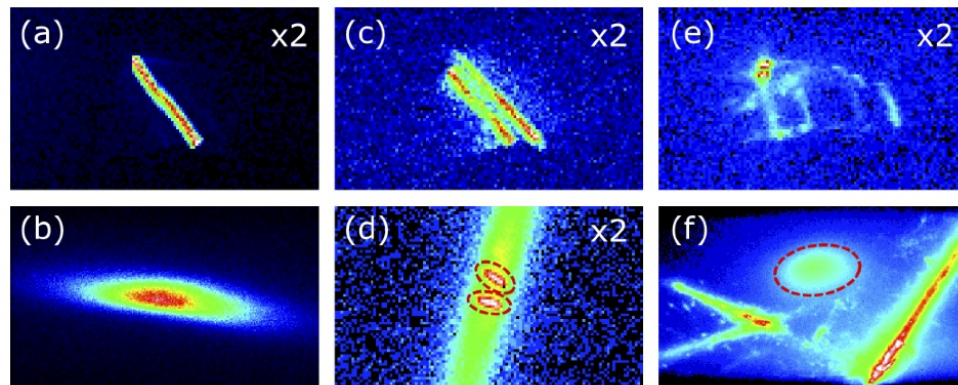
Figure 4.4: Some examples of measured diffraction signals, demonstrating the challenges encountered when trying to determine signal from background (from [57])

Some examples of measured diffraction signals with respect to various backgound are shown in Figure4.4. (a) illustrates a clean and sharp CTR signal while (b) is a broad CTR signal of a different structure. (c) and (d) show a split CTR signal caused by a sample miscut or with respect to a strongly anisotropic diffuse background. (e) is a strange signal shape caused by twining and microscopic faceting while (f) illustrates spurious signals originating from sample holder and bulk crystal, surrounding the real signal(marked by circle). [57]
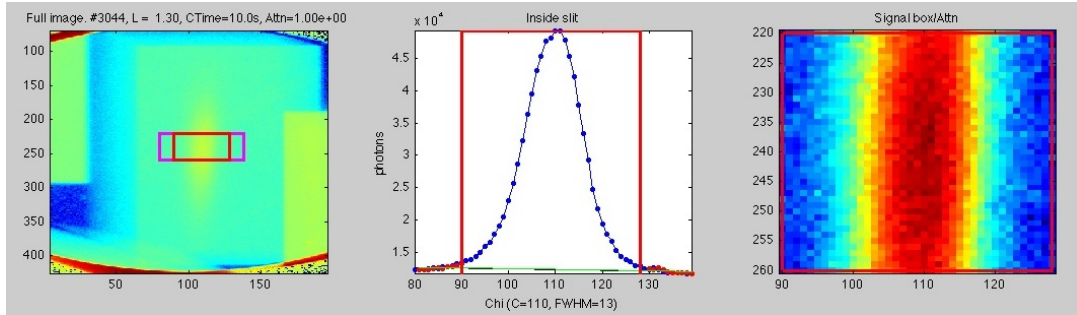
Figure 4.5: left: selection of signal/background box; middle: integration along pixels; right: image of signal inside of box

Figure 4.5 demonstrates data extraction process conducted by a MATLAB routine for a first-order superstructure rod. The signal stands out as a nice distinct peak while the background can be approximated as the part underneath the green straight line, which is subtracted from the intensity during the integration. For any set of (h, k), a sequence of such iteration is done to every raw detector image, i.e., at every measured value of l. Eventually the integrated intensity is plotted as a function of l.

Data correction

The measured intensities were corrected for background, active area, Lorentz, and polarization factors. We start with the differential scattering cross section, which can be written as [36]:

$$d\sigma/d\Omega = r_e^2 (A/A_u)|F_{hkl}|^2 Pu(Q), \tag{4.3}$$

where r_e is the classical electron radius, A is the active area, A_u is the area of the surface unit cell, F_{hkl} is the structure factor for a reflection with Miller indices hkl, P is the polarization factor, $u(Q)$ is a function that describes the line shape(eg. Lorentzian, Gaussian) and is normalized such that the integral over h and k is unity, and Q is the momentum transfer. The integrated intensity is the scattering cross

section integrated over all angles of freedom of the detector (eg. μ, ν).

Lorentz factor

Since $d\sigma/d\Omega$ is expressed in terms of Q, we need to change the angular integration variables into reciprocal space ones. The geometrical correction in integration volume is usually called the Lorentz factor (Vol. II of International Tables for X-ray Crystallography, 1995). It can be derived that $L = 1/sin\beta_{out}$ for grazing incident geometry, and $L = 1/\sin\beta_{in}$ for symmetric geometry. [36]

Polarization factor

The polarization factor P is given by $cos^2\alpha_{pol}$, with α_{pol} the angle that the direction of observation makes with the polarization direction. For the horizontal polarization component, $p_{hor} = z_{lab}$, and the vertical component $p_{ver} = x_{lab}$. Let p_h be the horizontal polarization fraction of the beam; the total polarization factor is then [36] [37]

$$P = p_h P_{hor} + (1 - p_h) P_{ver}. \qquad (4.4)$$

In experiments using synchrotron radiation the vertical polarization component is often neglected because the polarization is almost completely horizontal. For grazing incidence mode, we use $P_{hor} = 1 - (\cos\delta \sin\nu)^2$ and symmetric mode, $P_{hor} = (2\cos\beta_{in})^2$.

The incident-beam interception

Since the incident beam spills over the edges of the sample during the experiment, it is important to check the profile of the beam in the plane containing the incident and the specularly reflected beam, in order to correct the data for the fraction of the incident beam intercepted by the substrate surface. We wrote a numerical MATLAB code to apply the interception correction. [36] [37]

SXRD results

A total of 32 rods which include 15 CTRs and 17 SSRs were measured in the SXRD experiment. Surface symmetry reveals a $p31m$ pattern, and, after averaging over equivalents, we ended up with 8 unique rods - 4 CTRs and 4 SSRs. The range in reciprocal space used for subsequent analysis was $h, k = 0, ..., 3$ and $0.25 \leq l \leq 3.99$, with a sampling interval of 0.13 in $r.l.u$ along l.
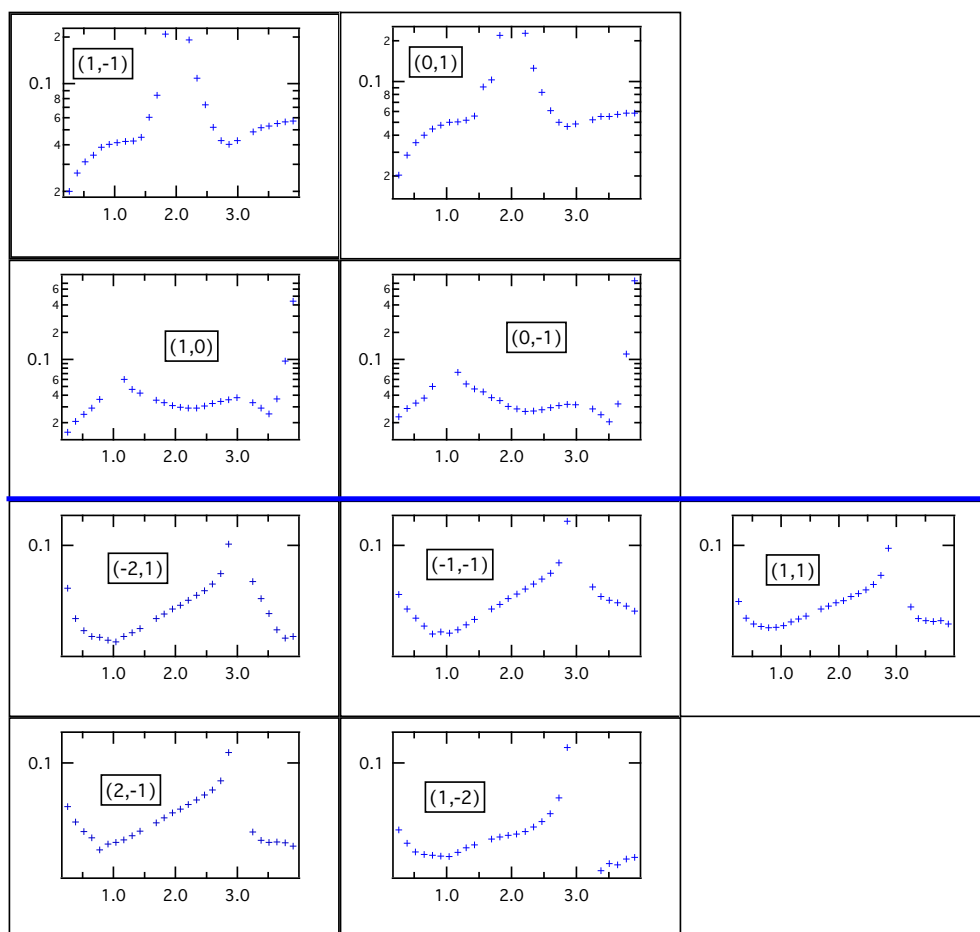
Figure 4.6: Crystal truncations rods acquired in SXRD experiments
top:first-order CTRs
bottom: second-order CTRs

Normalized structure factors plotted with varying l are presented in Figure4.6. The top section shows first-order CTRs acquired in the experiment, which reveals 3-fold symmetry for the 6 positions. (01)-like rods exhibit Bragg peaks at $l = 2$ and
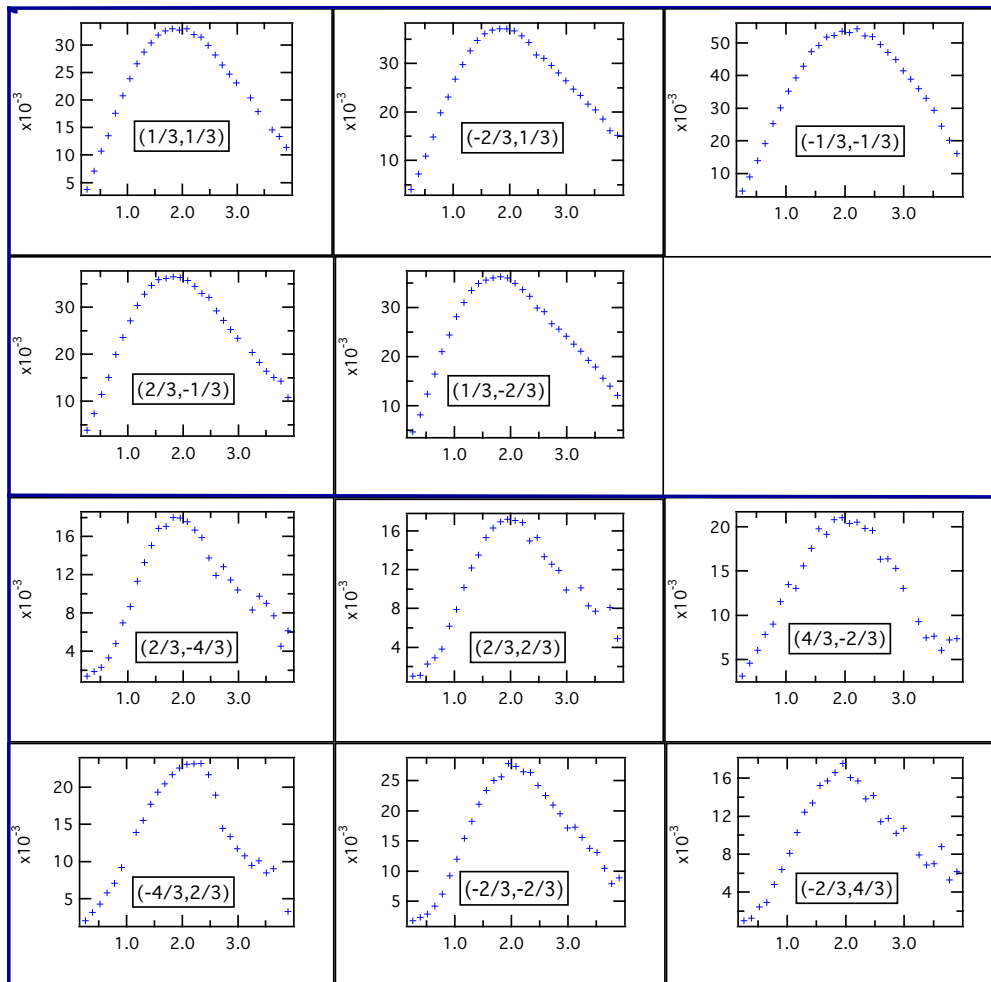
Figure 4.7: Super structure Rods acquired in SXRD experiments

(10)-like rods at $l = 1, 4$. The bottom section shows second-order CTRs, meaning (11)-like rods. As one can notice, all 5 rods share the same shape and peak at the same locations. Therefore, one may conclude that all second order CTRs are equivalent. The left lower panel displays third-order CTRs, again, distinct peaks locates at $l = 2$, and rods are equivalent.

Figure4.7 presents SSRs obtained from SXRD experiment. The first two rows show first-order SSRs which are all equivalent. The third and forth row show 5 equivalent second-order SSRs.

From the above discussion, it can be concluded that the reconstructed surface is $p31m$ type of symmetry group according to "International tables for X-ray Crystal-

lography".

Once all these corrections are made, the resulting E and σ(from equation 4.1 and 4.2) values are then representative of $|F|^2$, the square of the structure factor amplitude. While σ is a measure of the error in E due to counting statistics, it does not include systematic errors such as variation in the quality of the surface preparation and diffractometer misalignments. To determine these, it is important to take advantage of the surface symmetry by collecting several symmetry equivalents of each reflection, since these are made at very different angle settings and usually probe a different region of the surface; the systematic errors are represented in the variations of equivalent observations. Usually the number of equivalents sampled is too small for their standard deviation to be an accurate measure of the error, so some means of using the overall measurement statistics must be invented. [58]

Let the n repeated measurements of a given E be denoted $\{E_i, \sigma_i\}$ for $i = 1 \cdots n$ The weighted averages and standard deviation are

$$\tilde{E} = \sum_{i=1}^{n} \frac{E_i}{\sigma_i^2} \sum_{i=1}^{n} \frac{1}{\sigma_i^2} \tag{4.5}$$

$$\tilde{\sigma} = (\sum_{i=1}^{n} \frac{1}{\sigma_i^2})^{-1/2} \tag{4.6}$$

$$s = (\sum_{i=1}^{n} \frac{E_i}{\sigma_i^2} / \sum_{i=1}^{n} \frac{1}{\sigma_i^2} - \tilde{E}^2)^{1/2}. \tag{4.7}$$

Now consider each different reflections of the data set: assuming the systematic error to be a fixed proportion, it can be calculated as the ratio of s_j and intensity

$$\epsilon = \frac{1}{N} \sum_{\tilde{E} > 2\sigma_j} \frac{s_j}{E_j}, \tag{4.8}$$

where N is the number of measurements with $\tilde{E} > 2\tilde{\sigma}$ included in the sum: we only include sufficiently reliable measurements in the average. The final experimental

error in $\tilde{E}$ is now the quadrature sum of the random and systematic errors:

$$\tilde{\sigma}_j = (\tilde{\sigma}_j^2 + \epsilon^2 \tilde{E}_j^2)^{1/2}. \tag{4.9}$$

This formula can be used on all reflections, even those measured only once which have no s_j. Reflections observed to have $\tilde{E}_j < 0$ should be set to $\tilde{E}_j = 0$ first.

After obtaining the average over equivalent rods, final data with error bars were achieved. The systematic percentile error associated with the MgO(111) SXRD experiment is 14%. The set of 8 unique rods was used in the fitting process to explore the right model of atomic structure.

The relationship of error of intensity measured in the experiment to structure factor as used in calculation is derived below:

$$I = |F|^2 \tag{4.10}$$

$$\delta I = 2F\delta F \tag{4.11}$$

$$\frac{\delta I}{I} = 2\frac{\delta F}{F}. \tag{4.12}$$

The bulk of the MgO(111) lattice can be specified by 3 types of layers: ABC in fcc stacking. It is convenient to use a bulk unit cell in experiment; in that basis, all the CTR rods will have integer indices and SSRs will have fractional indices. A three-dimensional crystal can be described by specifying the contents of the simplest repeating unit and the way these repeating units stack to form the crystal. However, because of the reconstruction of the surface, the periodicity of crystal surface has changed. Therefore, instead of defining the unit cell as the original (1×1) bulk unit cell, a $(\sqrt{3} \times \sqrt{3})R30^o$ repeating unit can also be considered, a so called surface unit cell. The choice of either unit cell results in different (hk) indices, and the

transformation can be derived by a (2×2) matrix

$$M = \begin{bmatrix} 2 & 1 \\ -1 & 1 \end{bmatrix}$$

.

Now the bulk unit can be described as 6 layers of ABC stacking or 3 layers of Mg-O bilayer, whose positions in terms of fractions of unit cell lattice vectors are listed in Table4.1.

layers	atoms	x	y	z	layers	atoms	x	y	z
1	Mg	0	1/3	0	4	O	0	1/3	1/2
1	Mg	1/3	0	0	4	O	1/3	0	1/2
1	Mg	2/3	2/3	0	4	O	2/3	2/3	1/2
2	O	0	0	1/6	5	Mg	0	0	2/3
2	O	1/3	2/3	1/6	5	Mg	1/3	2/3	2/3
2	O	2/3	1/3	1/6	5	Mg	2/3	1/3	2/3
3	Mg	2/3	0	1/3	6	O	2/3	0	5/6
3	Mg	0	2/3	1/3	6	O	0	2/3	5/6
3	Mg	1/3	1/3	1/3	6	O	1/3	1/3	5/6

Table 4.1: MgO bulk unit cell, $a = 5.159\mathring{A}$, $b = 5.159\mathring{A}$, $c = 7.295\mathring{A}$, $\alpha = 90^o$, $\beta = 90^o$, $\gamma = 120^o$

4.4   Paterson function

A $3D$ partial Patterson function[ref: Sec 2] is computed using superstructure peaks and

$$P(\mu,\nu,\omega) = \sum\sum\sum F^2(hkl)cos[2\pi(h\mu + k\nu + l\omega)] \tag{4.13}$$

If there is a maximum of $P(\mu,\nu,\omega)$ at some point(μ,ν,ω), then there exist two atoms in the distribution whose distance apart is given by the vector (μ,ν,ω). Because no bulk relections are used in the calculation, only interatomic vectors present in the surface will arise. A contour map of the Patterson function in surface unit cell
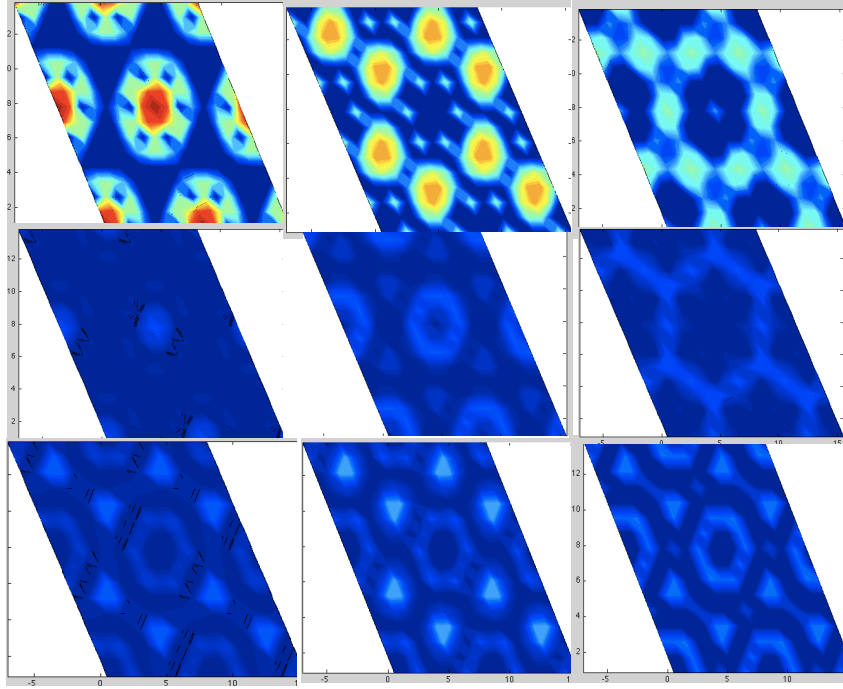
Figure 4.8: Inter-atomic correlation map

of each layer is shown in Figure 4.8. The strongest peaks are located at $(0, 1, 0)$, $(1, 1, 0)$ and $(1, 1, 0)$ (displayed in the first slide) which represent the atoms within the same layer. It agrees with the periodicity of a $\sqrt{3} \times \sqrt{3}$ unit cell. There are also some maxima at other ω values, representing interatomic vectors between atoms in different layers. Some slices with higher ω values show higher intensities than the slice lower than them. It can be implied that the atoms are fairly spread out in the z direction. Although the partial Patterson function will only show a subset of all the existing interatomic vectors as discussed below due to omitting negative peaks, it does not provide all the information needed to interpret the atomic structure of the reconstructed surface. [43]

For fractional order reflections, the in-plane Laue indices are

$$(h, k) = (m + \frac{1}{3}, n + \frac{2}{3}), or \tag{4.14}$$

$$(h, k) = (m + \frac{2}{3}, n + \frac{1}{3}) \tag{4.15}$$

where m and n are integers. Thus the cosine term in equation 4.13 is

$$\cos 2\pi[(m + \frac{1}{3})\mu + (n + \frac{2}{3})\nu], or \tag{4.16}$$

$$\cos 2\pi[(m + \frac{2}{3})\mu + (n + \frac{1}{3})\nu]. \tag{4.17}$$

Therefore μ and ν (corresponding to bulk lattice vectors) is positive only if $2\mu+4\nu$ or $4\mu + 2\nu$ is a multiple of three. These are the observed peaks $(\frac{1}{3}, \frac{2}{3})$, $(\frac{2}{3}, \frac{1}{3})$, $(0, 1)$ in Figure 4.8.

4.5 PARADIGM
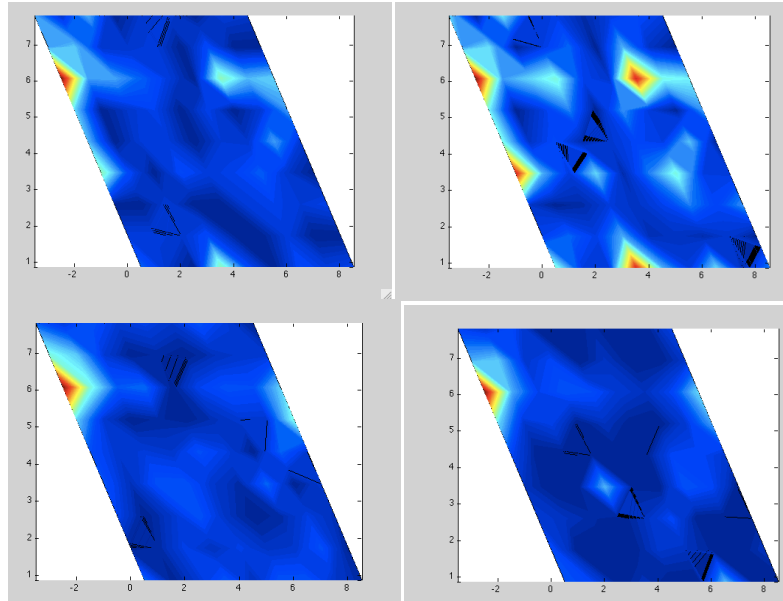
Figure 4.9: Electron density retrieved from PARADIGM

PARADIGM [ref: sec 2]retrieved four layers of electron density from the experimental data (Figure 4.9). The spacing between these layers can be calculated as

$$\Delta z = \frac{c}{l_{range}}, \tag{4.18}$$

where c is crystal parameter in the normal direction and l_{range} depends on the

range of l measured in the experiment, from 0.26 to 3.99.

$$l_{range} \quad = \quad 2 \times (3.99 - 0.26) = 7.46 \qquad (4.19)$$

$$\Delta z \quad = \quad 7.295\mathring{A}/7.46 = 0.98\mathring{A}. \qquad (4.20)$$

The interplanar separation of a MgO bulk is $1.216\mathring{A}$, therefore the resolution of the electron density should be sufficient to see each atomic layer. On the other hand, the electron density does not distinguish Mg from O, so there are more than one possible structure that can be derived from the result. Table 4.2 lists the possible models of the structure.

model I					model II				
layers	atoms	x	y	z	layers	atoms	x	y	z
1	Mg	0	2/3	0	1	O	0	2/3	0
2	O	2/3	2/3	1/6	2	Mg	0	1/3	1/6
2	O	1/3	0	1/6	2	Mg	1/3	0	1/6
2	O	0	1/3	1/6	2	Mg	2/3	2/3	1/6
2	O	0	2/3	1/6	2	Mg	0	2/3	1/6
3	Mg	0	2/3	1/3	3	O	0	2/3	1/3

Table 4.2: Possible models derived from PARADIGM

None of the above models result in a decent fit to the data. PARADIGM may have failed due to the improper accounting of multiple suface domains. [59] Unless multiple domains were considered in PARADIGM, seeking other methods of defining structural models is necessary.

4.6   GenX results

4.6.1   Introduction

Conventional refinement, such as ROD [45] is mainly operates by seeking for local minima by following the gradient of the goodness of fit. This approach has severe

limitation as it is prove to get stuck in local minima. The fitting program GenX, which is based on a differential genetic evolution search algorithm, is a good alternative to ROD. A detailed description can be found in previous chapter and other references. [ref: sec 2] Even though the experimental data set shows $p31m$ symmetry, the intensities of each rod need to be summed up incoherently in the calculation of structure factor. Instead of defining the symmetry operation in the simulation, a large set of data (25 rods) containing all the equivalent rods was used for refinement, thereby enforcing the symmetry of outcoming structure model.

In GenX, the figure of merit (FOM) is the function that compares how well the simulation matches the measured data. Strictly speaking , for Gaussian errors, a chi squared (χ^2) is the most appropriate. However, the world is never perfect and many times the data can be fitted more easily and more robustly if another FOM is chosen. Each FOM function has its merits and demerits, and fitting can rely critically on choosing the right FOM for the particular data set. As the models above, the FOM chosen is χ^2, which is a weighted function including error bars:

$$FOM_{\chi^2} = \frac{1}{N-1} \sum_i (\frac{Y_i - S_i}{\sigma_i})^2, \tag{4.21}$$

where Y_i represents experimental intensities, S_i is denoted as the corresponding simulations and N is the total number of data points.

Crystallographic R factor (denoted as R_1), gives the percentage of the summed structure factor residuals (absolute difference between data and simulation) over the entire data set with respect to the total sum of measured structure factors. For data sets spanning several orders of magnitude in intensity, R_1 is dominated by the residuals at high intensities, while large residuals at low intensities have very little impact on R_1. The square roots of the loaded intensities are taken for the calculation of R_1 in GenX:

$$FOM_{R_1} = \sum_i [\sqrt{(Y_i)} - \sqrt{(S_i)}] / \sum_i [\sqrt{(Y_i)}]. \tag{4.22}$$

The R_1 factor is not very sensitive to errors. As a rule of thumb, a large χ^2 indicates a poor fit. However $\chi^2 < 1$ indicates that the model is "over-fitting" the data(most likely the error variance has been overestimated). A $\chi^2 > 1$ indicates that the fit has not fully captured the data. In principle $\chi^2 = 1$ indicates that the extent of the match between observations and estimates is in accord with the error variance. A large R_1 factor also indicates a poor fit. $R_1 = 0$ means observations and estimates are identical, $R_1 = 1$ means statistically uncorrelated and $R_1 = 2$ is for anticorrelated spectra. [60].

4.6.2   Models

The structure of MgO(111) $(\sqrt{3} \times \sqrt{3})R30^o$ reconstructed surface has been studied by a few research groups before. Plass *etal* has reported cyclic ozone molecules bonded to the MgO surface, based on a transmission electron diffraction (TED). However the vertical spacing of the cyclic ozone over the second Mg layer can not be determined from two-dimensional TED data. TED combined with direct methods have been used by A. Subramanian and L.D. Marks [11]. They suggested that the surface was magnesium terminated, with two Mg vacancies in the first layer relative to a simple bulk terminated surface. The 2D symmetry of the surface structure is $p31m$ which is consistent with our experimental finding. However the fitting of this model to our experimental data is not very good.

As a first consideration, the intensities for superstructure rods of this model are significantly smaller than our experimental measurements. It can be suggested that the surface reconstruction is more complex than just vacancies in one topmost layer. Comparing the 00l rod, the periodicity does not agree. Therefore the relaxation of the reconstructed surface must be of a different form than what the model suggested.

The intensity of the specular rod (00l rod) as a function of l only depends on the inter-plane distance and the density of atoms. It gives essential and direct

information of the relaxation and vacancies of the surface. When fitting only the $00l$ rod while only the z positions were allowed to change, a good agreement between the experimental and simulated data was achieved, with χ^2 as low as 0.724. This result does not necessarily lead us to a unique complete model of reconstructed surface, but the nice agreement hints that this model is one of the possibilities.

layers	spacing	ratio to bulk spacing
1&2	1.216	1.00
2&3	1.420	1.16
3&4	1.637	1.34

Table 4.3: Interplanar spacing($\mathring{A}$) given by fitting only $00l$ rod.
$\chi^2 = 0.724$
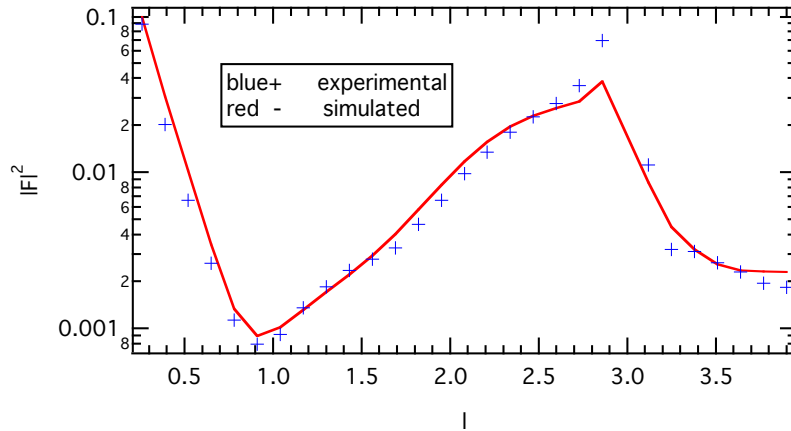
Figure 4.10: Specular Rod ($00l$ rod), Simulated vs Experimental

Figure 4.10 shows the simulated and experimental results. The model used in this simulation is based on L. Hammer's publication. [61] Hammer suggested a structure for CoO is based on a wurtzite bilayer on top of the cubic bulk layers. There was some relaxation among the topmost layers, but not significant for the layers closest to the bulk(Table 4.3).

A " stacking fault" structure is the next model considered according to chemistry intuition. In the model, the topmost layer of the bulk is rotated 180°. However if no lateral displacement occurred, this structure would not give rise to $(\frac{1}{3}, \frac{1}{3})$ like
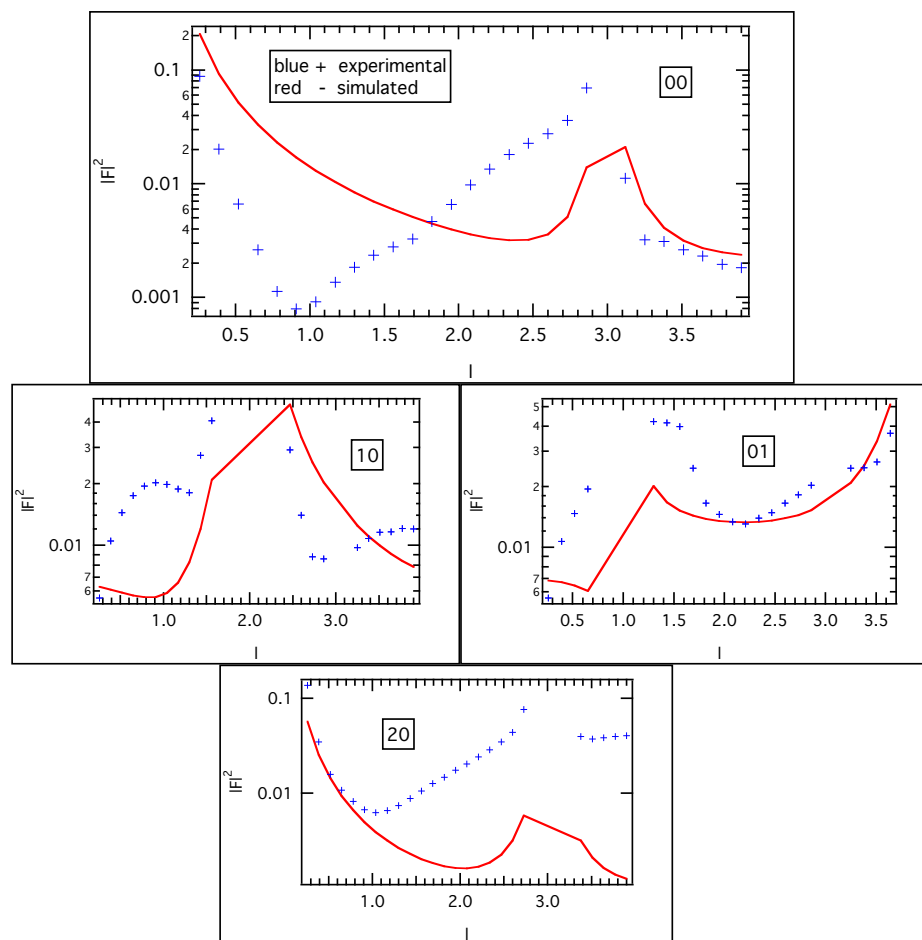
Figure 4.11: stacking fault results, Simulated vs Experimental
top: 00l rod; middle: first order CTR; buttom: second order CTR

intensities. Since the reconstructed sample is air-stable and long-lasting, the true
surface has to be a fairly stable structure. With the "stacking fault" formation,
there is no vacancy in the structure and it could also be energetically stable in the
presence of air.

Figure 4.11 displayed simulated intensities of "stacking fault" model together
with experimental data. Since there is no lateral displacement, the SSR intensities
are nearly zero. The top graph is 00l rod. The experimental data, between two Bragg
peaks, contains some modulation, which is lacking in the simulated graph. This
indicates that the reconstructed structure is most likely more than one monolayer
thick. The middle two graphs are first order CTRs. As shown, Bragg peaks are

well aligned while the detailed features do not agree for most of the data points, although it is possible some of the features are from the lateral displacement on the surface. Therefore, a better fit may be achievable trying to change the in-plane position. The bottom graph is the second order CTR. The low l fits fine but high l part is pretty distant from the reality.

GenX fitting on this model brings down the χ^2 to 7.85. Even though it still does not agree with the experimental measurements very well, it suggested the structure to change in a way that the inter-layer spacing is greater.

There are a group of polar (111) surfaces of the rocksalt oxides, such as NiO, CoO, MnO and MgO. [3] A *ab initio* study was carried out on MgO(111) and NiO(111) together for a (2×2) reconstruction. [56] This type of polar surface shares similar surface chemistry and mechanism. It was reported a coexistence model of rocksalt and wurtzite structure in CoO films. [61]. Since the $(\sqrt{3} \times \sqrt{3})$ reconstruction is close to a wurtzite structure, it is believable that this coexistence structure could also exist on the MgO(111) reconstructed surface. Moreover, the spacing normal to surface resulted from the $00l$ rod investigation also suggested a transition from MgO bulk spacing to a greater inter-layer distance. This structure also satisfies the $p31m$ symmetry as the experimental data. The χ^2 calculated directly from the published model and experimental data is 9.43. A few adjustments were made to optimize the fit.

The first adjustment is to allow each plane move freely in the z direction and let atoms in the top three monolayers free except for constraints imposed by the symmetry. The χ^2 reduced to 5.53. Bond lengths are shown in Table 4.4. As comparing the results(see Figure 4.13), the simulated SSRs do not have as much intensity as the experimental measurements, but the periodicities agreed. One of the reasons that the fit is not very good is possibly that this model is a single domain. According to the size and morphological study of the sample, it is unlikely
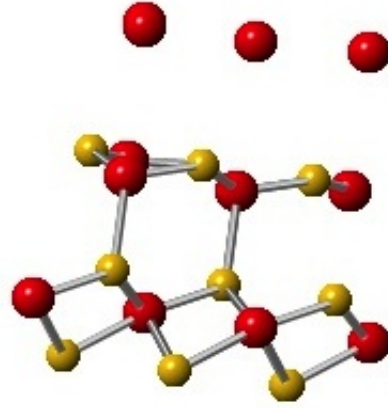
Figure 4.12: Single-domain model

that the entire reconstructed surface is only a single domain.

Mg-O bilayers	bond	bond length
1&2	$Mg_1 - O_1$	2.11
1&2	$Mg_2 - O_2$	2.11
1&2	$Mg_3 - O_3$	2.11
2&3	$Mg_1 - O_1$	1.92
2&3	$Mg_2 - O_2$	1.92
2&3	$Mg_2 - O_2$	1.92
3&4	$Mg_1 - O_1$	2.19
3&4	$Mg_2 - O_2$	2.19
3&4	$Mg_3 - O_3$	2.56
4&5	$Mg_1 - O_1$	1.72
4&5	$Mg_2 - O_2$	1.79
4&5	$Mg_3 - O_3$	1.79

Table 4.4: Nearest neighbor bond length of single-domain model($\mathring{A}$), $\chi^2 = 5.53$)

The next adjustment is introducing multiple domains in the model. Two scenarios can satisfy the symmetry of the whole surface: symmetric domains but each domain has asymmetric structure; the other scenario is each domain has symmetric structure; and domains are simply steps or some morphologically related features, since the $p31m$ symmetry more than a three-fold symmetry but less than a six-fold. A rotational matrix is applied to the computation to introduce domains. The
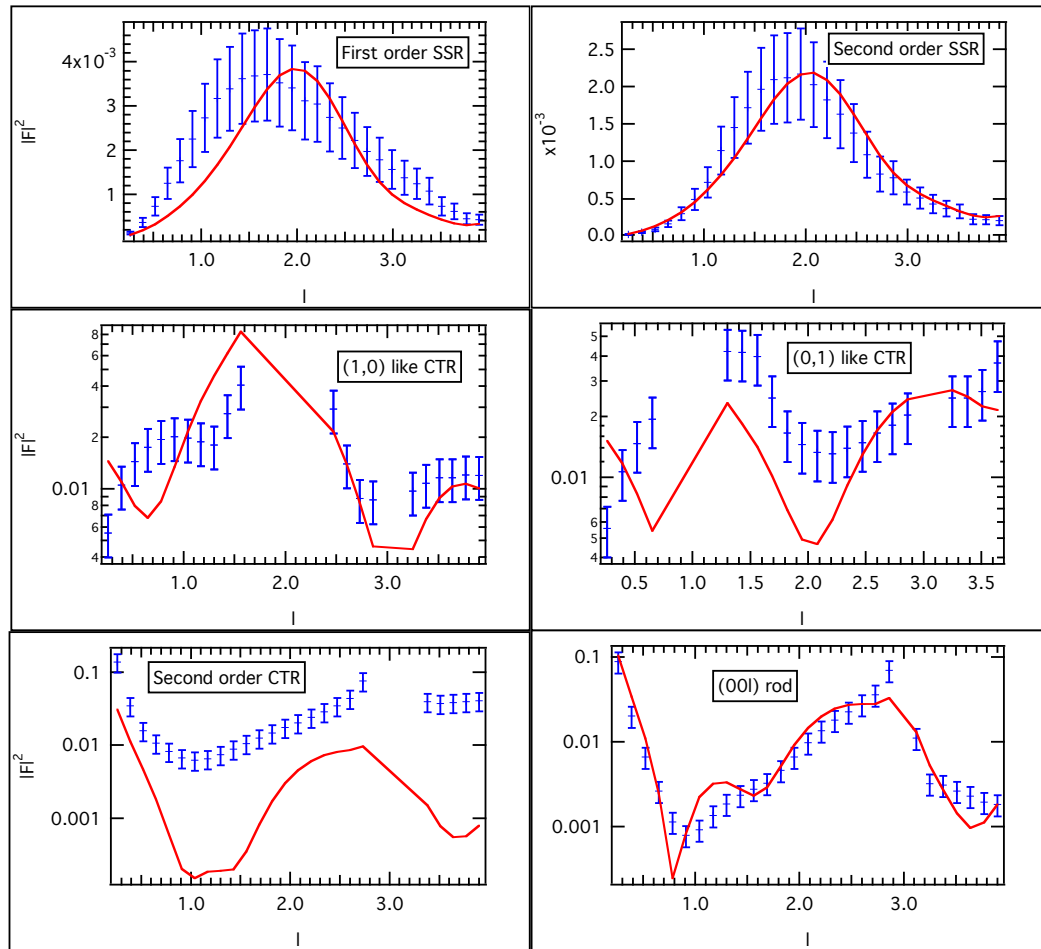
Figure 4.13: Single-domain results, Simulated vs Experimental
top:first order SSR; middle: first order CTR; bottom left: second order CTR, bottom right: $00l$ rod

three-fold matrix is

$$M_1 = \begin{bmatrix} 1 & 0 \\ 0 & 1 \end{bmatrix}; M_2 = \begin{bmatrix} 0 & -1 \\ 1 & -1 \end{bmatrix}; M_3 = \begin{bmatrix} -1 & 1 \\ -1 & 0 \end{bmatrix}$$

.

and six-fold matrix is

$$M_1 = \begin{bmatrix} 1 & 0 \\ 0 & 1 \end{bmatrix}; M_2 = \begin{bmatrix} 1 & -1 \\ 1 & 0 \end{bmatrix}; M_3 = \begin{bmatrix} 0 & -1 \\ 1 & -1 \end{bmatrix}$$

$$M_4 = \begin{bmatrix} -1 & 0 \\ 0 & -1 \end{bmatrix}; M_5 = \begin{bmatrix} -1 & 1 \\ -1 & 0 \end{bmatrix}; M_6 = \begin{bmatrix} 0 & 1 \\ -1 & 1 \end{bmatrix}$$

.
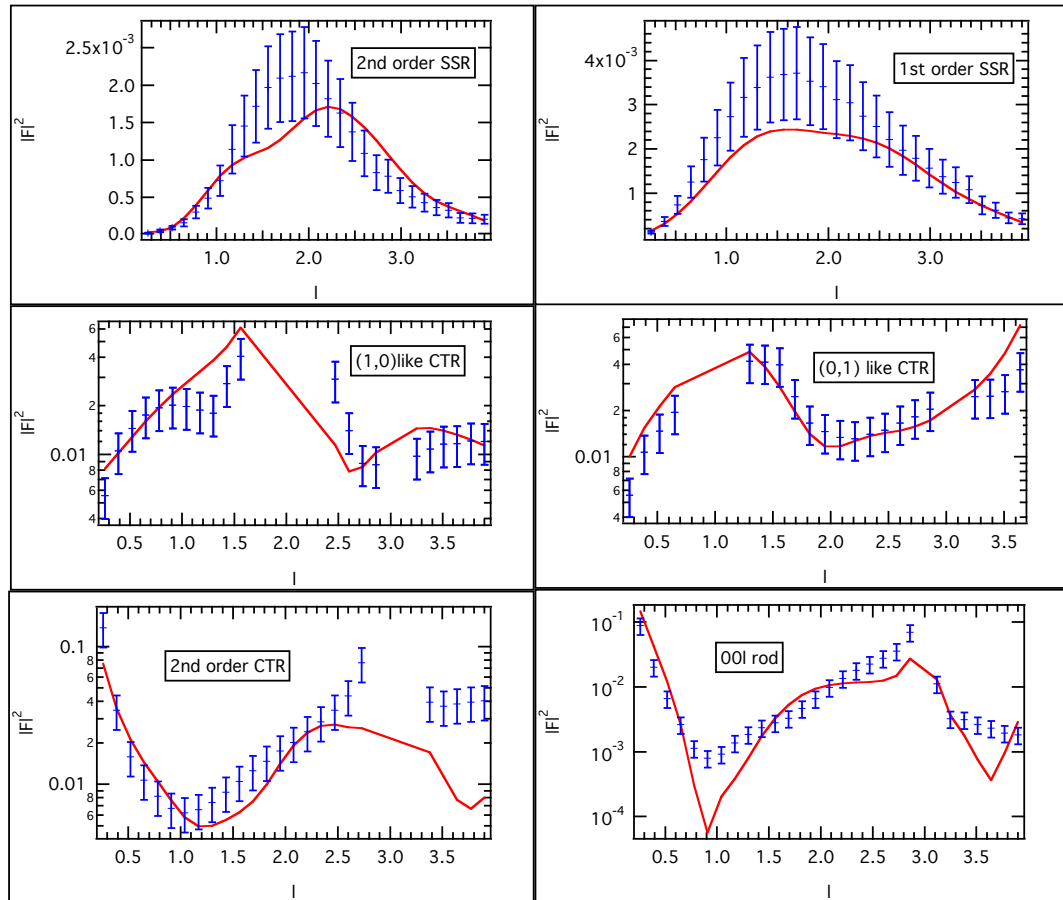
Figure 4.14: Three-domain simulation vs experimental data, $\chi^2 = 1.493$
Top row: SSR results
Middle row: first order CTR
Bottom left: second order CTR; bottom right : specular ($00l$) rod

The three domains of the surface structure will guarantee a three fold symmetry and six domains will have a six fold symmetry. The experimental data has symmetry that is higher than three fold but lower than six fold. Both three-fold rotational and six-fold rotational domains can both lead to data with $p31m$ symmetry. The fitting parameter χ^2 of models with domains is significantly lower compared with other ones, so surface with multiple domains is a more reasonable structure. χ^2 of

three-domain model is 1.9 fitted with GenX when keeping atoms in the same plane moving together in the z direction (except for the topmost layer) and allowing atoms move freely in the lateral direction for the top four layers. χ^2 decreased to 1.493 when letting the top six layers move freely. Comparing the simulated data with measured data, shown in Figure 4.14, there is still some disagreement but it is the best fit among all the models. Table 4.6 gives the three-dimension displacements of each atom in the top bilayer. As an example, "O31dy" means the y-direction displacement of the first O atom in third layer. Table 4.7 shows the surface unit cell fractional coordinates of the three domain model.

layers	spacing	ratio to bulk spacing
1&2	1.216	1.00
2&3	1.216	1.00
3&4	1.462	1.20
4&5	1.436	1.18

Table 4.5: Three-domain model interplanar spacing($\mathring{A}$), $\chi^2 = 1.493$

atoms	displacements	atoms	displacements	atoms	displacements
$O31dy$	-0.1998	$O31dx$	0.0914	$O31dz$	-0.0195
$O32dy$	-0.1917	$O32dx$	0.0954	$O32dz$	-0.0195
$O33dy$	-0.1966	$O33dx$	0.0834	$O33dz$	-0.0195
$Mg31dy$	-0.1949	$Mg31dx$	0.0300	$Mg31dz$	0.1129
$Mg32dy$	-0.1984	$Mg32dx$	0.0232	$Mg32dz$	0.1605
$Mg33dy$	-0.1955	$Mg33dx$	0.0288	$Mg33dz$	0.1605
$O21dy$	-0.0058	$O21dx$	-0.0469	$O21dz$	-0.0496
$O22dy$	-0.0084	$O22dx$	-0.0481	$O22dz$	-0.0496
$O23dy$	-0.0085	$O23dx$	-0.0523	$O23dz$	-0.0496
$Mg21dy$	0.0293	$Mg21dx$	0.0766	$Mg21dz$	0.0002
$Mg22dy$	0.0355	$Mg22dx$	0.0721	$Mg22dz$	0.0002
$Mg23dy$	0.0322	$Mg23dx$	0.0738	$Mg23dz$	0.0002

Table 4.6: Atomic displacements of three-domain model($\mathring{A}$), $\chi^2 = 1.493$

Figure 4.15 displays the visualization of the three-domain model. It consists the same structure for each domain, and three domains are 120° rotationally apart. The first two layers are closest to the bulk unit. They still keep the rock salt

atoms	x	y	z
Mg11	0.6866	0.6789	0
Mg12	0.0269	0.3501	0
Mg13	0.3601	0.0151	0
O11	0.2530	0.6010	0.1668
O12	0.5850	0.2682	0.1668
O13	0.9160	0.9295	0.1668
Mg21	0.7434	0.0293	0.3334
Mg22	0.0721	0.7021	0.3334
Mg23	0.4071	0.3655	0.3334
O21	0.9531	0.3275	0.5338
O22	0.2852	0.9915	0.5338
O23	0.7388	0.6582	0.5338
Mg31	0.7580	0.468	0.7306
Mg32	0.4287	0.8083	0.7306
Mg33	0.0834	0.1367	0.7306
O31	0.3565	0.4682	1.1606
O32	0.0288	0.8045	1.1606
O33	0.6967	0.1384	0.9462

Table 4.7: Surface unit cell fractional coordinates of three-domain model, (a=5.159$\mathring{A}$, b=5.159$\mathring{A}$, c=7.295$\mathring{A}$) χ^2 = 1.493

structure. The third layer and above the structure transform to a wurtzite hexagonal shape. The entire surface unit is expanded compared with bulk unit. There is large relaxation- twice as large as the original interplanar distance. This implies that there is some electron density on the top of the surface which can possibly be ordered adsorbates. Table 4.5 shows the interplanar spacing of this model, except for the topmost layer where atoms show buckling. Table 4.8 presents the bond length of such model. Some of the bonds are 1.73$\mathring{A}$, which is a little short for this bond.

The six-domain model failed to reveal a χ^2 as low as the three-domain model, χ^2 = 3.1. Moreover, all the atoms in each layer are free to move in any x and y individually; once the three atoms in one layer move away from their symmetric position it will break the $p31m$ symmetry of the surface. This will more likely to be the case if the given initial model is far away from the real model, GenX will lead the result to an unrealistic model. Upon this point, it proves in some way that the

Mg-O bilayers	bond	bond length
1&2	$Mg_1 - O_1$	1.74
1&2	$Mg_2 - O_2$	1.73
1&2	$Mg_3 - O_3$	1.74
2&3	$Mg_1 - O_1$	1.73
2&3	$Mg_2 - O_2$	1.76
2&3	$Mg_2 - O_2$	1.74
3&4	$Mg_1 - O_1$	2.00
3&4	$Mg_2 - O_2$	2.25
3&4	$Mg_3 - O_3$	2.18
4&5	$Mg_1 - O_1$	1.77
4&5	$Mg_2 - O_2$	2.04
4&5	$Mg_3 - O_3$	2.04

Table 4.8: Nearest neighbor bond length of three-domain model($\mathring{A}$), $\chi^2 = 1.493$

layers	spacing	ratio to bulk spacing
1	1.216	1.00
2	1.179	0.96
3	1.350	1.10
4	1.052	0.86

Table 4.9: Three-domain model interplanar spacing($\mathring{A}$), $R_1 = 0.170$

three-domain is closer to the real model of the reconstructed surface structure.

Seeking the best fit and the most optimized model, a few models are also fitted using the R_1 FOM. Results are compared for these two FOM.

Table 4.9 presents the interplanar spacing of the resultant model from R_1 factor fitting in GenX, $R_1 = 0.170$. The first four layers of atoms were kept from rumpling (moved together), while the topmost layer atoms have more freedom in the z direction. The best fitted model shows a different normal to surface spacing than the previously presented model. There were alternating expansion and contractions between layers through out the unit. Displacements of all the atoms are shown in Table 4.10 and the surface unit cell fractional coordinates are shown in Table 4.11

A comparison of simulated data and experimental data is shown in Figure 4.16. Because error bars were not taken into account in the calculation, the simulation
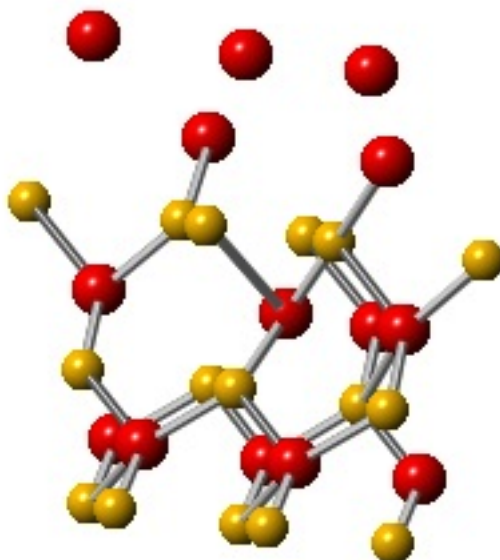
Figure 4.15: Three-domain model, χ^2 = 1.493

conforms to experimental data slightly better than the χ^2 fit. Although the $00l$ rod does not agree very well, the spacing between layers will need more investigation. The bondlengths (Table 4.12) are closer to that of bulk in this fitting process.

There are both advantage and disadvantage in the two choices of FOM. The χ^2 fit shows a better statistical result and the R_1 factor fit gives a more physical model in the aspect of bondlength . In any sense, the three-domain model seems to be the most reasonable model, and as found out it is a transformation from rock salt (111) stacking to a wurtzite formation.

4.7   Conclusion

In conclusion, the $\mathrm{MgO}(111)$ $\sqrt{(3)} \times \sqrt{(3)} R30^o$ reconstructed surface has been studied using LEED, afterward SXRD. The SXRD data have been fit with several algorithm including GenX. The differential evolution algorithm have optimized a few reasonable starting atomic structural models. The best result is given by the coexistence of rock salt and wurtzite structure. Two different fitting parameters were

atoms	displacements	atoms	displacements	atoms	displacements
$O31dy$	−0.1999	$O31dx$	0.1003	$O31dz$	−0.0822
$O32dy$	−0.1999	$O32dx$	0.0985	$O32dz$	−0.1053
$O33dy$	−0.1997	$O33dx$	0.1108	$O33dz$	−0.0811
$Mg31dy$	−0.1827	$Mg31dx$	0.1072	$Mg31dz$	0.0289
$Mg32dy$	−0.1957	$Mg32dx$	0.0866	$Mg32dz$	-0.0548
$Mg33dy$	−0.1997	$Mg33dx$	0.0769	$Mg33dz$	-0.0537
$O21dy$	−0.0089	$O21dx$	−0.0490	$O21dz$	−0.0719
$O22dy$	−0.0041	$O22dx$	−0.0447	$O22dz$	−0.0662
$O23dy$	0.0022	$O23dx$	0.0022	$O23dz$	−0.0613
$Mg21dy$	0.0609	$Mg21dx$	0.1162	$Mg21dz$	-0.0393
$Mg22dy$	0.0614	$Mg22dx$	0.1194	$Mg22dz$	-0.0369
$Mg23dy$	0.0621	$Mg23dx$	0.1199	$Mg23dz$	-0.0349

Table 4.10: Atomic displacements of three-domain model($\mathring{A}$), R_1 = 0.170

utilized for the refinement process, which gives χ^2 = 1.493 and R_1 = 0.170. Even though the real physical structure might need more pondering in the aspect of chemical bonding, this study has achieved an atomic-scale understanding of the reconstructed polar surface.

atoms	x	y	z
Mg11	0.6667	0.6667	0
Mg12	0.3333	0.0000	0
Mg13	0.0000	0.3333	0
O11	0.3333	0.6667	0.1668
O12	0.6667	0.3333	0.1668
O13	0.0000	0.0000	0.1668
Mg21	0.7299	0.1194	0.3274
Mg22	0.0777	0.7966	0.3274
Mg23	0.4012	0.4446	0.3274
O21	0.9986	0.2972	0.5534
O22	0.2988	0.9443	0.5534
O23	0.6717	0.6289	0.5534
Mg31	0.4708	0.7866	0.7280
Mg32	0.1347	0.1200	0.7280
Mg33	0.8020	0.4269	0.7280
O31	0.4734	0.3904	0.9244
O32	0.1689	0.7857	1.1540
O33	0.8004	0.0479	0.9262

Table 4.11: Surface unit cell fractional coordinates of three-domain model, (a=5.159$\mathring{A}$, b=5.159$\mathring{A}$, c=7.295$\mathring{A}$) $R_1 = 0.170$

Mg-O bilayers	bond	bond length
1&2	$Mg_1 - O_1$	2.11
1&2	$Mg_2 - O_2$	2.11
1&2	$Mg_3 - O_3$	2.11
2&3	$Mg_1 - O_1$	1.75
2&3	$Mg_2 - O_2$	1.75
2&3	$Mg_2 - O_2$	1.79
3&4	$Mg_1 - O_1$	2.05
3&4	$Mg_2 - O_2$	1.93
3&4	$Mg_3 - O_3$	2.06
4&5	$Mg_1 - O_1$	1.95
4&5	$Mg_2 - O_2$	1.90
4&5	$Mg_3 - O_3$	1.94

Table 4.12: Nearest neighbor bond length of three-domain model($\mathring{A}$), $R_1 = 0.170$
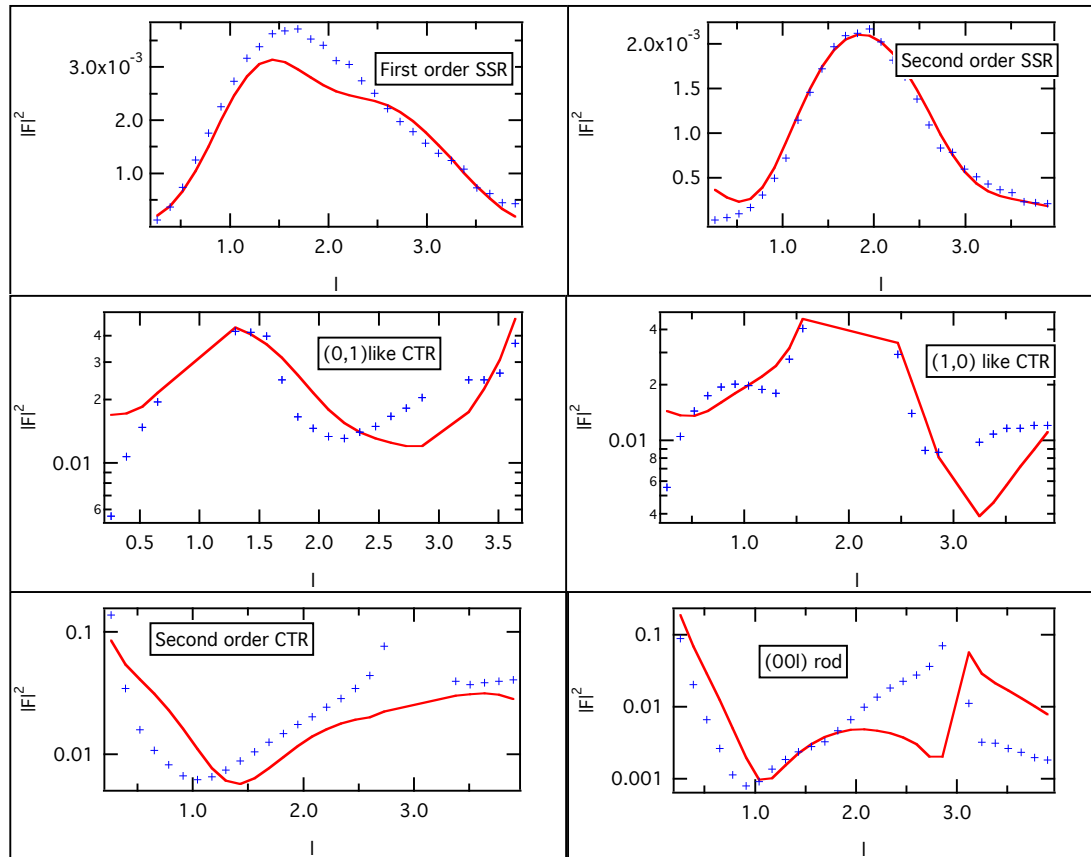
Figure 4.16: Experimental data vs simulated data, $R_1 = 0.170$
top: SSR
middle: first order CTR
buttom left: second order CTR, buttom right: 00l rod

Chapter 5

Water on reconstructed MgO(111)

5.1   Introduction

Chemical reactions at the solid-water interface play an important role in numerous processes, from environmental systems to the biological availability and geochemical studies. [62] [63] An atomic-scale study of solid-liquid interface structure is required to properly understand physical and chemical phenomena such as crystal growth from solution, lubrication, and electrochemistry. [64] [65]For a long time, studies of interfacial processes at model surfaces have been hampered by the limited molecular knowledge of the aqueous interface structure. Using a third-generation x-ray source is one of the feasible methodologies to probe such an interface.

Initial studies focused on the effect of the water medium on the structure and relaxation of the mineral itself [66]. Later studies probed the adsorption of dilute species (ML quantities) on mineral surfaces [67] and eventually the speciation of water near the crystal surface. A number of recent studies have shown that water at the interface may show ordering that is significantly different from bulk water molecular arrangements. [68] [69] [62] The liquid near the interface is constrained by the periodic potential of the crystal surface and is expected to show more ordering than in the bulk liquid.

The layering of the liquid in the direction perpendicular to the surface has been observed in a few cases [70] [64] [65]. However, it is more difficult to detect the amount of in-plane ordering of the liquid on the surface. The presence or absence of lateral ordering may be expected to alter the chemical pathway followed for

subsequent mineral-water reactions (ie., hydroxylation) [71] [64] or crystal growth [64]. The aim of the experiment was to investigate whether a reconstructed mineral surface may serve as a template to induce pronounced lateral ordering in the near-surface water layers as well as to determine the degrees of ordering at the surface. This determination can shed light on whether physical (as opposed to chemical) factors are operant in the formation of ice-like layers. Reconstructed MgO(111) substrates were employed as model minerals. Each may be formed with and without a$\sqrt{(3)} \times \sqrt{(3)}R30^o$reconstruction under controlled circumstance, allowing a direct comparison of the template effect.

5.2   Experiments

The process of preparing MgO(111) reconstructed surface is identical to that previous chapter: double-sided polished MgO 10×10 mm single crystals were placed between two MgO wafers, and annealed in a tube furnace at 1000^oC for 30 hrs. SXRD experiments were conducted on the MgO(111)$\sqrt{(3)} \times \sqrt{(3)}R30^o$ reconstructed surface in three environments: crystal truncation rods (CTR) and superstructure rods (SSR) were acquired under dry ambient conditions, with a thin layer of bulk water over the surface, and enclosed in an evacuated beryllium dome. For the measurements with water, a thin Kapton film was used to compress a water layer over the sample. This Kapton was also present for our measurements on the dry surface for direct comparison of the results. Measurements were also taken for comparison when the sample was dried by blowing the water from the sample surface. The experiments were conducted on the 33ID beamline at Advanced Photon Sources (APS), Argonne National Laboratory. Measurements were performed on a reconstructed single-crystal surface at 12.5 keV photon energy and at a fixed incidence angle of 0.1^o to reduce scattering from the bulk.

Lattice constants used as the input of experiments are $a = 2.978\mathring{A}, b = 2.978\mathring{A}, c = $

$7.295\mathring{A}, \alpha = 90^o, \beta = 90^0, \gamma = 120^o$, which describes a MgO(111) 1×1 bulk lattice. The h and k indices are chosen to describe the in-plane momentum transfer in reciprocal-lattice units of the MgO(111) reconstruction, and l for the perpendicular momentum transfer.

5.3   Results and discussion

Preliminary comparison reveals first, although the background signal was greatly increased due to scattering by the water layer, air, and Kapton foil, the periodic peaks were distinguishable and robust. This reconstruction is stable under water and both CTR and SSR peaks were accessible using an area detector. Second, features appear specifically for SSR intensity in presence of water, which must occur at the lateral length scale of the reconstructed surface template. In fact, the modulation period (in l) has essentially been halved. As this (hk) Fourier component is not found in the bulk, this indicates that the thickness of the layer having this lateral periodicity has approximately doubled. Moreover, modulation of a CTR in the presence of water (see Figure 5.1) was also observed at certain l values. With the area detector at APS, second order SSR can be detected and peaks stand out clearly from the increased background; as do all of the features for fractional order measurements (see Figure 5.2).

The blown dried surface after water treatment did not recover to its original dry state, which indicates the water molecule has a irreversible interaction with the reconstructed surface. The modulation which arised with presence of water disappeared when the surface is blown dry. This implies that the additional layer of thickness that had the same lateral periodicity as the surface reconstruction was part of the water layer, that is, the interfacial water layer exhibited lateral ordering. The $\sqrt{(3)} \times \sqrt{(3)}R30^o$ reconstruction remains after water is removed, again proved that the reconstruction is stable both in air and water.

5.4 Conclusion

The water/MgO(111) liquid-solid interface has been studied by surface X-ray diffraction. Preliminary results confirm that the ordering of liquid on the surface is a few monolayers thick, possibly double that of the unreconstructed bulk. The $\sqrt{(3)} \times \sqrt{(3)}R30^o$ reconstruction is stable under water and the factional peaks are detected as robust and clear.
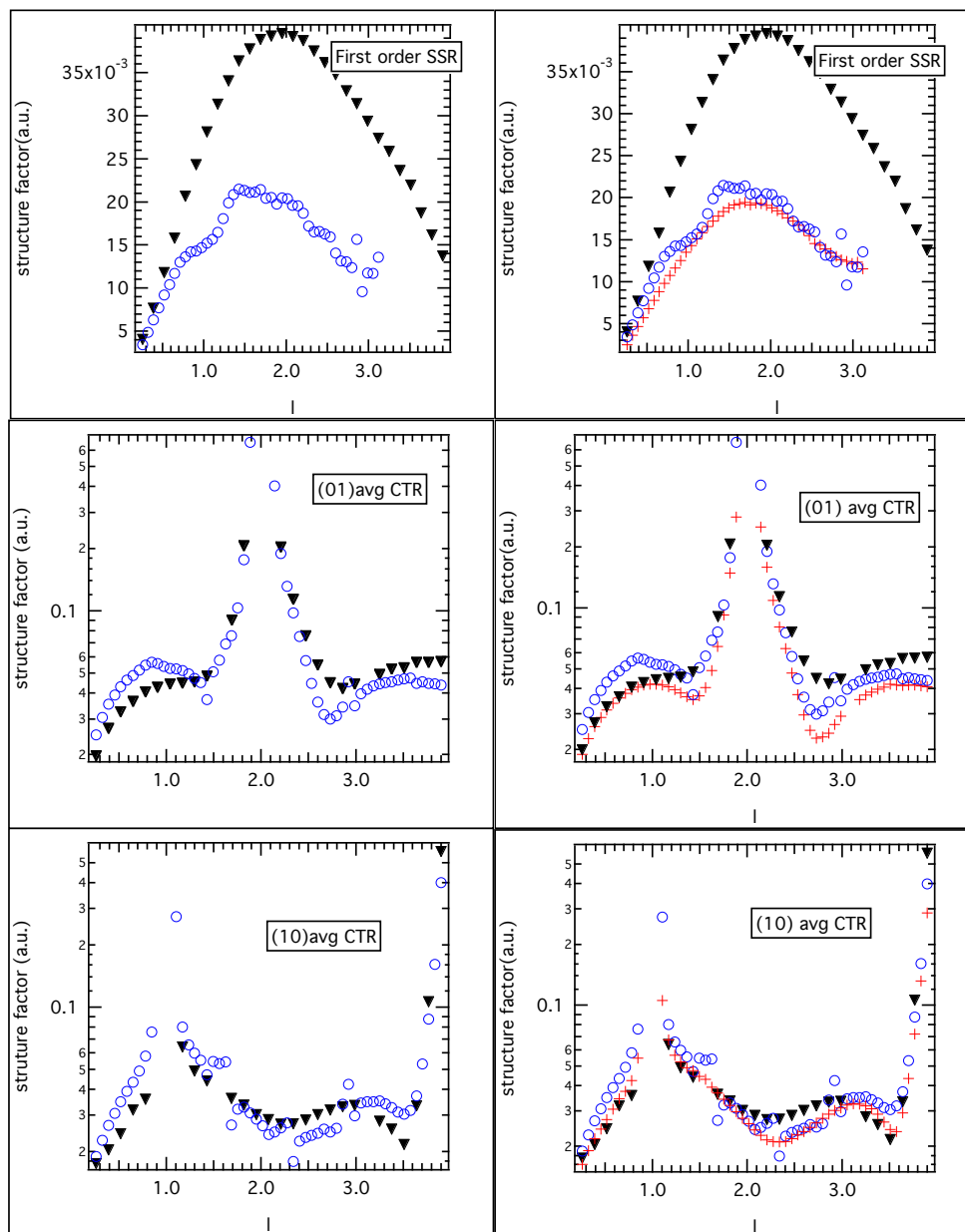
Figure 5.1: Left: comparison of dry and wet surfaces of $\sqrt{(3)} \times \sqrt{(3)} R30^o$ reconstructed MgO(111) surface
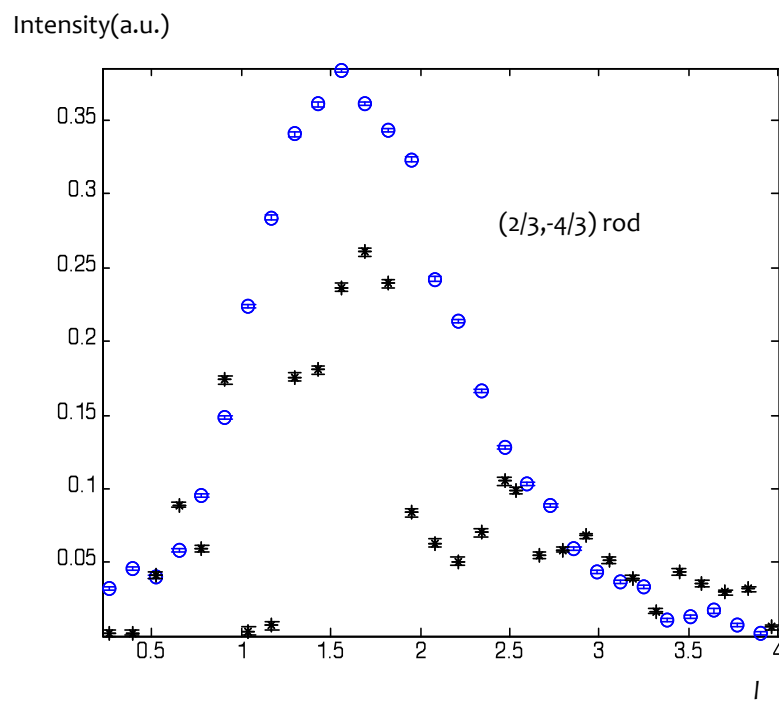right: comparison of $\sqrt{(3)} \times \sqrt{(3)} R30^o$ reconstructed MgO(111) under three environments(see text)

Intensity(a.u.)

Figure 5.2: comparison of second order SSR dry and wet $\sqrt{(3)} \times \sqrt{(3)}R30^o$ reconstructed surface

Chapter 6

$ZnO(000\bar{1})$ surface analysis $\&$ Surface X-ray diffraction

6.1 Introduction

Zinc Oxide (ZnO), due to its large bandgap of 3.3 eV (at $300K$) and high exciton binding energy (60 meV), has drawn great attention as a potential material for blue and ultraviolet optical and electrical devices. [72] It has been shown by experiments as well that ZnO is very resistant to high-energy radiation, making it a suitable candidate for applications in space. [73] As the starting point for understanding a wide range of surface phenomena, quantitative surface structural information can lead to many useful properties of materials, such as electronic structure of surface and interface, heterogeneous catalytic processes. [2] Meanwhile, many properties of the material depend on its polarity, for example, growth, etching, defect generation and plasticity, spontaneous polarization, and piezoelectricity. [72] [74]

In wurtzite ZnO, associated directions $< 000\bar{1} >$ are the most commonly used surface and direction for growth. The oxygen-terminated $ZnO(000\bar{1})$ surface forms when wurtzite ZnO crystal is cleaved parallel to the basal plane, and O atoms are located at the vacuum side of the as-cleaved surface.

The $ZnO(000\bar{1})$ surface has been widely observed to display a (1×1) symmetry. [75] Reconstructions on clean, Zn-polar ZnO surfaces have been reported. [76] Theoretical research has been done as well for ZnO surfaces with hydrogen. [77] We have discovered that, upon annealing to $1100^{o}C$ in atmosphere or low-hydrogen UHV conditions, an air-stable $\sqrt{(}3) \times \sqrt{(}3)R30^{o}$reconstruction results, as shown

by low-energy electron diffraction (LEED) analysis. X-ray photoelectron spectroscopy shows no surface contamination, indicating that the reconstruction is intrinsic. [26] To determine the structure of the reconstruction, we performed surface x-ray diffraction on an air-annealed sample at the 33-ID-XOR/UNI beamline, Argonne National Laboratory. Both crystal truncation rods (CTR) and surface structure rods (SSR) have been measured and the results are presented. With further analysis and investigation, we expect to understand the atomic structure of the $ZnO(000\bar{1})\sqrt{(3)} \times \sqrt{(3)}R30^o$ surface reconstruction.

6.2   Experiments

To prepare reconstructed surface, double-sided polished ZnO 5×10mm single crystals (obtained from CrysTec Corporations) were ultrasonically cleaned in acetone and methanol, respectively 15 minutes, and then blown dry with inert gas. ZnO wafers were stacked together with alternating O and Zn terminated surfaces attached. The sample stack, left in an alumina crucible, was loaded into a closed-end tube furnace and annealed at 1100^oC for approximately 48 hours.

After annealing, samples were mounted into an ultra high vacuum (UHV) chamber for LEED and XPS analysis. Repeating ion sputtering is needed sometimes inside of the UHV chamber, followed by annealing to achieve order. Samples to be prepared in situ were mounted to a Ta sample holder with "W"-shape clips, inserted into UHV, Ar$^+$ sputtered for 30 min, then annealed at 650^oC for 15 min. After one to three such cycles, a reconstructed structure was investigated by low energy electron diffraction (LEED).

In the LEED experiment, fractional order spots are observed within the (1×1) unit cell, corresponding to a $\sqrt{(3)} \times \sqrt{(3)}R30^o$ reconstruction. The XPS spectra show only features pertaining to O and Zn, indicating a clean surface. [26]

Surface X-ray diffraction was conducted at the 33-ID-XOR/UNI beamline, Ar-

Figure 6.1: CTR measurements of ZnO $\sqrt{(3)} \times \sqrt{(3)}R30^o$ reconstructed surface
left column: first order CTR
middle column: second order CTR
right column: third order CTR

gonne National Laboratory. Both crystal truncation rods (CTR) and surface structure rods (SSR) have been measured (Figure 6.1, Figure 6.2). Lattice constants used as the input of experiments are $a = 3.253\mathring{A}, b = 3.253\mathring{A}, c = 5.313\mathring{A}, \alpha = 90^o, \beta = 90^0, \gamma = 120^o$, which describes a $\mathrm{ZnO}(000\hat{1})1 \times 1$ bulk lattice. The h and k indices are chosen to describe the in-plane momentum transfer in reciprocal-lattice units of the $\mathrm{ZnO}(000\hat{1})1 \times 1$ reconstruction, and l for the perpendicular momentum transfer. Therefore integer (hk) sets are CTRs and fractional order (hk) sets are SSRs.
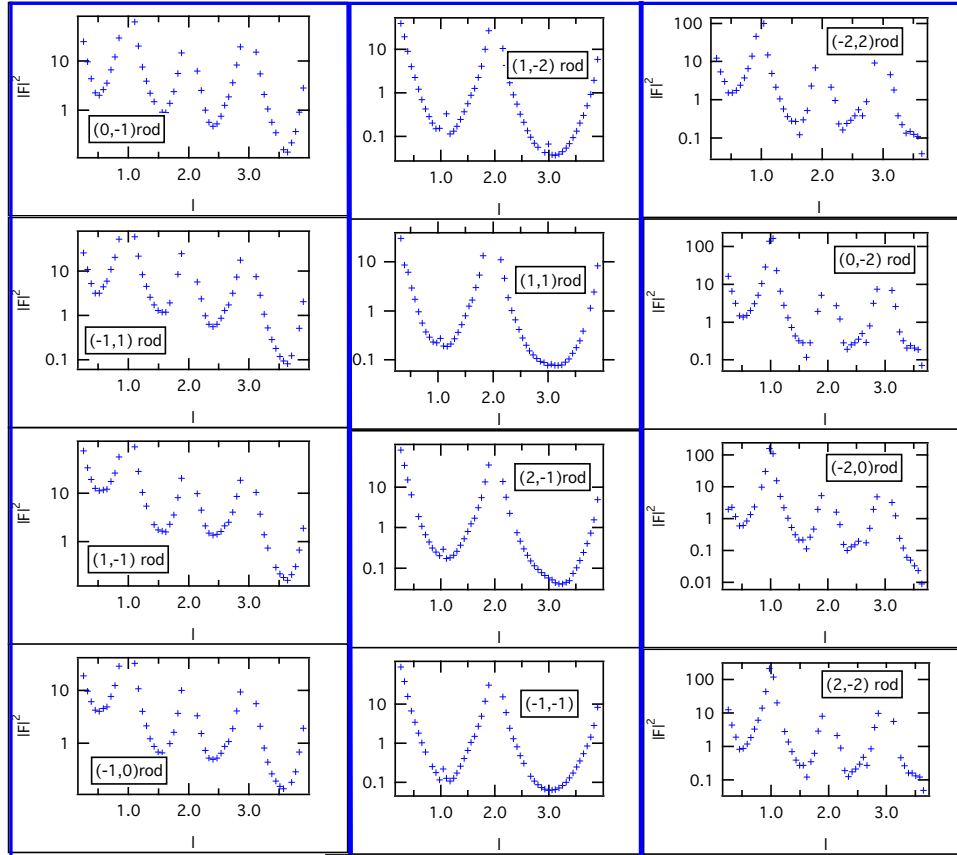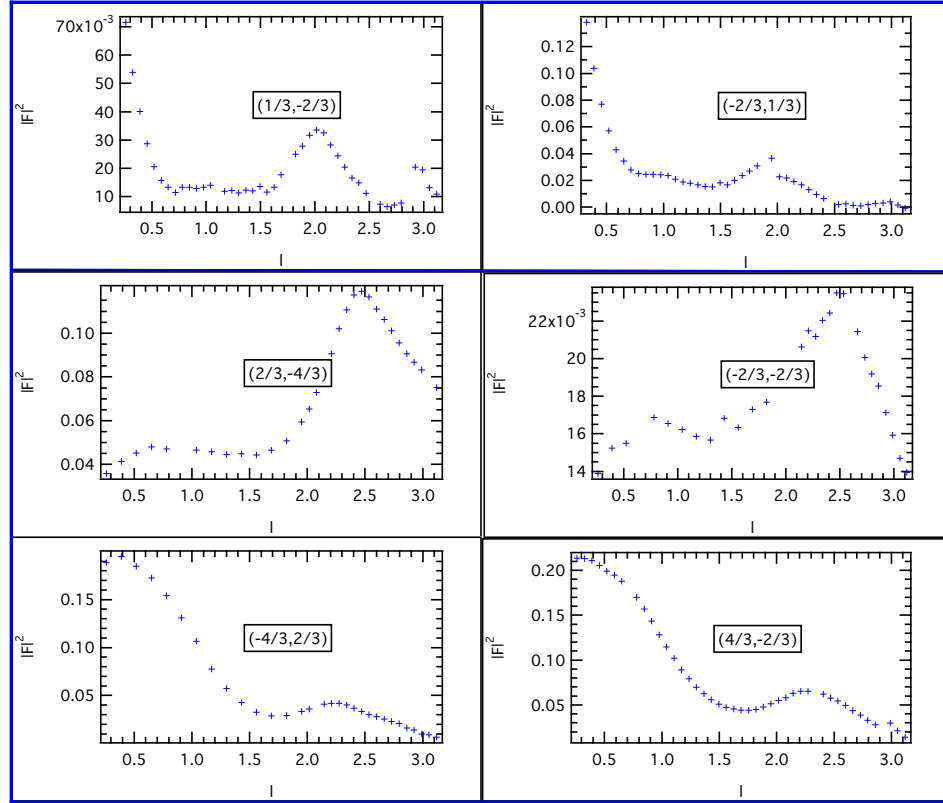
Figure 6.2: SSR measurements of ZnO $\sqrt{(3)} \times \sqrt{(3)}R30^o$ reconstructed surface
top row: first order SSR
middle and bottom row: second order SSR and two types of equivalence

6.3   Results and discussion

In figure6.1, the first order four CTR rods are close to identical, so are the second and third order CTR rods. So considering the bulk spots, the surface shows a six-fold symmetry. The SSR rods presents a different result. the second order SSR suggested a mirror symmetry while first order might be a three fold symmetry. Overall, it is suggested that the surface has a symmetry lower than six fold and it is highly possible that the symmetry is caused by multiple domains. All the above obervations can be useful determining the structure of the surface after correction of the intensities.

Moreover, the SSRs all show strong modulation which indicates that the surface reconstruction is more than one monolayer. The periodicity of the modulations in l

is at the order of $\Delta l \approx 2$, this would indicate that the thickness of the reconstructed

layer $\Delta z = \frac{2\pi}{\Delta l c^*}$ is about 3.067 $\mathring{A}$.

Bibliography

[1] Claudine Noguera. *Physics and Chemistry at Oxide Surfaces*. Cambridge University Press, 1996.

[2] D.P. Woodruff. Solved and unsolved problems in surface structure determination. *Surface Science*, 500(1-3):147–171, March 2002.

[3] Claudine Noguera. Polar oxide surfaces. *Journal of Physics: Condensed Matter*, 12(31):R367–R410, 2000.

[4] Juncheng Hu, Kake Zhu, Lifang Chen, Christian Kübel, and Ryan Richards. MgO(111) Nanosheets with Unusual Surface Activity. *The Journal of Physical Chemistry C*, 111(32):12038–12044, August 2007.

[5] R Angew. *Manipulation of Nanoscale Materials: An Introduction to Nanoarchitectonics*. Royal Society of Chemistry, 2012.

[6] Hiroshi Onishi, Chikashi Egawa, Tetsuya Aruga, and Yasuhiro Iwasawa. Adsorption of Na atoms and oxygen-containing molecules on MgO(100) and (111) surfaces. *Surface Science*, 191(3):479–491, 1987.

[7] Richard Plass, Kenneth Egan, Chris Collazo-Davila, Daniel Grozea, Eric Landree, Laurence Marks, and Marija Gajdardziska-Josifovska. Cyclic Ozone Identified in Magnesium Oxide (111) Surface Reconstructions. *Physical Review Letters*, 81(22):4891–4894, November 1998.

[8] Vlado K. Lazarov, Zhuhua Cai, Kenta Yoshida, K. Honglian L. Zhang, M. Weinert, Katherine S. Ziemer, and Philip J. Hasnip. Dynamically Stabilized Growth of Polar Oxides: The Case of MgO(111). *Physical Review Letters*, 107(5):056101, July 2011.

[9] P Bruno and C Chappert. Ruderman-Kittel theory of oscillatory interlayer exchange coupling. *Physical review. B, Condensed matter*, 46(1):261–270, July 1992.

[10] Eric Fullerton, M. Conover, J. Mattson, C. Sowers, and S. Bader. Oscillatory interlayer coupling and giant magnetoresistance in epitaxial Fe/Cr(211) and (100) superlattices. *Physical Review B*, 48(21):15755–15763, December 1993.

[11] a Subramanian, L D Marks, O Warschkow, and D E Ellis. Direct observation of charge transfer at a MgO(111) surface. *Physical Review Letters*, 92(2):026101, January 2004.

[12] Shih-Chia Chang and Peter Mark. The crystallography of the polar (0001) Zn and (0001)O surfaces of zinc oxide. *Surface Science*, 46(1):293–300, November 1974.

[13] Jules D. Levine, A. Willis, W.R. Bottoms, and Peter Mark. Correlation of electronic, leed, and auger diagnostics on ZnO surfaces. *Surface Science*, 29(1):144–164, 1972.

[14] L. Fiermans, E. Arijs, J. Vennik, and W. Maenhout-Van Der Vorst. A combined LEED, AES and XPS study of the ZnO {0001} polar surfaces. *Surface Science*, 39(2):357–367, 1973.

[15] H. van Hove and R. Leysen. LEED study on the polar surfaces of ZnO. *Physica Status Solidi (a)*, 9(1):361–367, January 1972.

[16] R. Leysen, G. van Orshaegen, H. van Hove, and A. Neyens. Electronic and structural characteristics of ZnO (0001) surfaces. *Physica Status Solidi (a)*, 18(2):613–621, August 1973.

[17] Shih-Chia Chang and Peter Mark. The crystallography of the principal non-polar (1120) and (1010) surfaces of zinc oxide. *Surface Science*, 45(2):721–727, October 1974.

[18] Gregory S. Rohrer and Dawn A. Bonnell. The geometric and electronic structure of the ZnO(0001) surface. *Surface Science Letters*, 247(1):L195–L200, 1991.

[19] T.M. Parker, N.G. Condon, R. Lindsay, F.M. Leibsle, and G. Thornton. Imaging the polar (0001) and non-polar (1010) surfaces of ZnO with STM. *Surface Science*, 415(3):L1046–L1050, 1998.

[20] C.B. Duke and A.R. Lubinsky. Calculations of low-energy electron diffraction intensities from the polar faces of ZnO. *Surface Science*, 50(2):605–614, June 1975.

[21] Mauro Sambi, Gaetano Granozzi, Gian Andrea Rizzi, Maurizio Casarin, and Eugenio Tondello. An angle-scanned photoelectron diffraction study on the surface relaxation of ZnO (0001). *Surface Science*, 319(1):149–156, 1994.

[22] N Jedrecy, M Sauvage-Simkin, and R Pinchaux. The hexagonal polar ZnO(0001)-(11) surfaces: structural features as stemming from X-ray diffraction. *Applied Surface Science*, 162:69–73, 2000.

[23] a Wander and N M Harrison. The stability of polar oxide surfaces: The interaction of H[sub 2]O with ZnO(0001) and ZnO(0001). *The Journal of Chemical Physics*, 115(5):2312, 2001.

[24] Olga Dulub, Ulrike Diebold, and G. Kresse. Novel Stabilization Mechanism on Polar Surfaces: ZnO(0001)-Zn. *Physical Review Letters*, 90(1):016102, January 2003.

[25] B. K. Meyer, H. Alves, D. M. Hofmann, W. Kriegseis, D. Forster, F. Bertram, J. Christen, A. Hoffmann, M. Straß burg, M. Dworzak, U. Haboeck, and A. V. Rodina. Bound exciton and donoracceptor pair recombinations in ZnO. *physica status solidi (b)*, 241(2):231–260, February 2004.

[26] S.T. King, S.S. Parihar, K. Pradhan, H.T. Johnson-Steigelman, and P.F. Lyman. Observation of a (33)R30 reconstruction on O-polar ZnO surfaces. *Surface Science*, 602(22):L131–L134, November 2008.

[27] A. Seubert, K. Heinz, and D. Saldin. Direct determination by low-energy electron diffraction of the atomic structure of surface layers on a known substrate. *Physical Review B*, 67(12):125417, March 2003.

[28] Luth. Luth (1997) Surfaces and interfaces of solid materials.

[29] G Renaud. Oxide surfaces and metal/oxide interfaces studied by grazing incidence X-ray scattering. *Surface Science Reports*, 32(1-2):5–90, 1998.

[30] I. Robinson. Crystal truncation rods and surface roughness. *Physical Review B*, 33(6):3830–3836, March 1986.

[31] R. Feidenhans'l. Surface structure determination by X-ray diffraction. *Surface Science Reports*, 10(3):105–188, 1989.

[32] J. Bohr, R. Feidenhans'l, M. Nielsen, M. Toney, R. Johnson, and I. Robinson. Model-Independent Structure Determination of the InSb(111)22 Surface with Use of Synchrotron X-Ray Diffraction. *Physical Review Letters*, 54(12):1275–1278, March 1985.

[33] R. Feidenhansl, F. Grey, R. Johnson, S. Mochrie, J. Bohr, and M. Nielsen. Oxygen chemisorption on Cu(110): A structural determination by x-ray diffraction. *Physical Review B*, 41(8):5420–5423, March 1990.

[34] D. P. Woodruff and T. A. Delchar. *Modern Techniques of Surface Science.* Cambridge University Press, 1994.

[35] Jens Als-Nielsen and Des McMorrow. *Elements of Modern X-ray Physics(Google eBook).* John Wiley & Sons, 2011.

[36] E Vlieg. Integrated Intensities Using a Six-Circle Surface X-ray Diffractometer. *Journal of Applied Crystallography*, 30(5):532–543, October 1997.

[37] C M Schlepütz, R Herger, P R Willmott, B D Patterson, O Bunk, Ch Brönnimann, B Henrich, G Hülsen, and E F Eikenberry. Improved data acquisition in grazing-incidence X-ray scattering experiments using a pixel detector. *Acta crystallographica. Section A, Foundations of crystallography*, 61(Pt 4):418–25, July 2005.

[38] I K Robinson and D J Tweet. Surface X-ray diffraction. *Reports on Progress in Physics*, 55(5):599–651, May 1992.

[39] Jianwei Miao, Pambos Charalambous, Janos Kirz, and David Sayre. Extending the methodology of X-ray crystallography to allow imaging of micrometre-sized non-crystalline specimens. 400(6742):342–344, July 1999.

[40] D K Saldin, R J Harder, V L Shneerson, and W Moritz. Phase retrieval methods for surface x-ray diffraction. *Journal of Physics: Condensed Matter*, 13(47):10689–10707, November 2001.

[41] P.F. Lyman, V.L. Shneerson, R. Fung, S.S. Parihar, H.T. Johnson-Steigelman, E.D. Lu, and D.K. Saldin. Structure and stability of Sb/Au(110)-c(22) surface phase. *Surface Science*, 600(2):424–435, January 2006.

[42] R Fung, V L Shneerson, P F Lyman, S S Parihar, H T Johnson-Steigelman, and D K Saldin. Phase and amplitude recovery and diffraction image generation method: structure of Sb/Au(110)-radical3xradical3R54.7 degrees from

surface X-ray diffraction. *Acta crystallographica. Section A, Foundations of crystallography*, 63(Pt 3):239–50, May 2007.

[43] A. Patterson. A Fourier Series Method for the Determination of the Components of Interatomic Distances in Crystals. *Physical Review*, 46(5):372–376, September 1934.

[44] H Lipson and WC FRS. The determination of crystal structure. 1966.

[45] Elias Vlieg. ROD : a program for surface X-ray crystallography. *Journal of Applied Crystallography*, 33(2):401–405, April 2000.

[46] John H. Holland. *Adaptation in natural and artificial systems: An introductory analysis with applications to biology, control, and artificial intelligence.*

[47] Rainer Storn and Kenneth Price. Differential Evolution A Simple and Efficient Heuristic for global Optimization over Continuous Spaces. *Journal of Global Optimization*, 11(4):341–359, December 1997.

[48] M. Wormington, C. Panaccione, K. M. Matney, and D. K. Bowen. Characterization of structures from X-ray scattering data using genetic algorithms. *Philosophical Transactions of the Royal Society A: Mathematical, Physical and Engineering Sciences*, 357(1761):2827–2848, October 1999.

[49] Matts Björck and Gabriella Andersson. GenX : an extensible X-ray reflectivity refinement program utilizing differential evolution. *Journal of Applied Crystallography*, 40(6):1174–1178, November 2007.

[50] Andrew Nelson. Co-refinement of multiple-contrast neutron/X-ray reflectivity data using MOTOFIT. *Journal of Applied Crystallography*, 39(2):273–276, March 2006.

[51] Samantha Y Chong and Maryjane Tremayne. Combined optimization using Cultural and Differential Evolution: application to crystal structure solution from powder diffraction data. *Chemical communications (Cambridge, England)*, (39):4078–80, October 2006.

[52] R. Bennett, N. McCavish, M. Basham, V. Dhanak, and M. Newton. Structure of Adsorbed Organometallic Rhodium: Model Single Atom Catalysts. *Physical Review Letters*, 98(5):056102, February 2007.

[53] S A Pauli, S J Leake, M Björck, and P R Willmott. Atomic imaging and direct phase retrieval using anomalous surface x-ray diffraction. *Journal of physics. Condensed matter : an Institute of Physics journal*, 24(30):305002, August 2012.

[54] J Martínez-Blanco, V Joco, C Quirós, P Segovia, and E G Michel. Surface x-ray diffraction analysis using a genetic algorithm: the case of Sn/Cu(100)-[Formula: see text]. *Journal of physics. Condensed matter : an Institute of Physics journal*, 21(13):134011, April 2009.

[55] Dieter Wolf. Reconstruction of NaCl surfaces from a dipolar solution to the Madelung problem. *Physical Review Letters*, 68(22):3315–3318, June 1992.

[56] a. Wander, I. Bush, and N. Harrison. Stability of rocksalt polar surfaces:An ab initio study of MgO(111) and NiO(111). *Physical Review B*, 68(23):233405, December 2003.

[57] Christian M Schlep. Systematic Structure Investigation of YBCO Thin Films with Direct Methods and Surface X-ray Diffraction.

[58] I.K. Robinson. Handbook on Synchrotron Radiation 1991 Robinson.pdf.

[59] D K Saldin, R J Harder, V L Shneerson, and W Moritz. Surface x-ray crystallography with alternating constraints in real and reciprocal space: the case of mixed domains. *Journal of Physics: Condensed Matter*, 14(16):4087, 2002.

[60] Home Search, Collections Journals, About Contact, My Iopscience, and I P Address. Surface X-ray diffraction. 599.

[61] W. Meyer, D. Hock, K. Biedermann, M. Gubo, S. Müller, L. Hammer, and K. Heinz. Coexistence of Rocksalt and Wurtzite Structure in Nanosized CoO Films. *Physical Review Letters*, 101(1):016103, July 2008.

[62] Kunaljeet S. Tanwar, Cynthia S. Lo, Peter J. Eng, Jeffrey G. Catalano, Donald A. Walko, Gordon E. Brown, Glenn A. Waychunas, Anne M. Chaka, and Thomas P. Trainor. Surface diffraction study of the hydrated hematite (1102) surface. *Surface Science*, 601(2):460–474, 2007.

[63] Colleen M Hansel, Shawn G Benner, Jim Neiss, Alice Dohnalkova, Ravi K Kukkadapu, and Scott Fendorf. Secondary mineralization pathways induced by dissimilatory iron reduction of ferrihydrite under advective flow. *Geochimica et Cosmochimica Acta*, 67(16):2977–2992, 2003.

[64] M. Reedijk, J. Arsic, F. Hollander, S. de Vries, and E. Vlieg. Liquid Order at the Interface of KDP Crystals with Water: Evidence for Icelike Layers. *Physical Review Letters*, 90(6):066103, February 2003.

[65] J. Arsic, D. Kaminski, P. Poodt, and E. Vlieg. Liquid ordering at the Brushite-{010}water interface. *Physical Review B*, 69(24):245406, June 2004.

[66] Ronald P Chiarello, Roy A Wogelius, and Neil C Sturchio. In-situ synchrotron X-ray reflectivity measurements at the calcite-water interface. 1993.

[67] Y Qian, N. Sturchio, R. Chiarello, P. Lyman, T. Lee, and M. Bedzyk. Lattice location of trace elements within minerals and at their surfaces with X-ray standing waves. *Science*, 265(5178):1555–1557, September 1994.

[68] Paul Fenter and Neil C. Sturchio. Mineralwater interfacial structures revealed by synchrotron X-ray scattering. *Progress in Surface Science*, 77(5):171–258, 2004.

[69] Jeffrey G. Catalano, Zhan Zhang, Changyong Park, Paul Fenter, and Michael J. Bedzyk. Bridging arsenate surface complexes on the hematite (012) surface. *Geochimica et Cosmochimica Acta*, 71(8):1883–1897, 2007.

[70] Aparna Pareek, Xavier Torrelles, Klaus Angermund, Jordi Rius, Uta Magdans, and Hermann Gies. Structure of interfacial water on fluorapatite (100) surface. *Langmuir : the ACS journal of surfaces and colloids*, 24(6):2459–64, March 2008.

[71] Marija Gajdardziska-Josifovska and Renu Sharma. Interaction of oxide surfaces with water: environmental transmission electron microscopy of MgO hydroxylation. *Microscopy and microanalysis : the official journal of Microscopy Society of America, Microbeam Analysis Society, Microscopical Society of Canada*, 11(6):524–33, December 2005.

[72] U. Ozgur, Ya. I. Alivov, C. Liu, A. Teke, M. A. Reshchikov, S. Dogan, V. Avrutin, S.-J. Cho, and H. Morkoc. A comprehensive review of ZnO materials and devices. *Journal of Applied Physics*, 98(4):041301, 2005.

[73] D. C. Look, D. C. Reynolds, J. W. Hemsky, R. L. Jones, and J. R. Sizelove. Production and annealing of electron irradiation damage in ZnO. *Applied Physics Letters*, 75(6):811, 1999.

[74] Nishuang Liu, Guojia Fang, Wei Zeng, Hai Zhou, Hao Long, Xiao Zou, Yuping Liu, and Xingzhong Zhao. High performance ZnO nanorod strain driving transistor based complementary metal-oxide-semiconductor logic gates. *Applied Physics Letters*, 97(24):243504, 2010.

[75] a. Wander, F. Schedin, P. Steadman, a. Norris, R. McGrath, T. Turner, G. Thornton, and N. Harrison. Stability of Polar Oxide Surfaces. *Physical Review Letters*, 86(17):3811–3814, April 2001.

[76] M. Kunat, St. Gil Girol, Th. Becker, U. Burghaus, and Ch. Wöll. Stability of the polar surfaces of ZnO: A reinvestigation using He-atom scattering. *Physical Review B*, 66(8):081402, August 2002.

[77] Georg Kresse, Olga Dulub, and Ulrike Diebold. Competing stabilization mechanism for the polar ZnO(0001)-Zn surface. *Physical Review B*, 68(24):245409, December 2003.

CURRICULUM VITAE

Wei Han

Place of birth: Xiaogan, Huibei, P.R. China

Education

B.S. University of science and technology of China, June 2005

Major: Physics

PhD University of Wisconsin Milwaukee, May 2014

Major: Physics

Dissertation Title: Surface x-ray diffraction study on polar oxide surface and interface

Research Experience

Research Assistant   September 2007-present

University of Wisconsin-Milwaukee

- Conducted Surface x-ray diffraction (SXRD) experiments on reconstructed polar oxide surface and liquid-solid interface at Brookhaven National Laboratory/Argonne National Laboratory with synchrotron x-ray source, 6 circle diffractometer and PLATUS area detector controlled by SPEC macro system.Achieved precise experimental data with limited time and training.
- Analyzed reconstructed polar oxide surface using Low energy electron diffraction (LEED) and X-ray photoelectron Spectroscopy (XPS) in Ultra high vacuum (UHV) chamber.Became expert in UHV system and adjunct equipments.
- Created data analysis computer models using open source code written in C++ (from European Synchrotron Radiation Facility (ESRF)) and Python, coded in MATLAB for large amount data management and error statistics.
- Characterized material surface with various equipments such as SEM, AFM.

Teaching Assistant   September 2007- present

University of Wisconsin- Milwaukee

- Taught undergraduate Physics courses. Tutored high school Advanced Placement Physics, GRE Quantitative, general college Physics (all majors).

Publication

In preparation: Wei Han and Paul Lyman, "Liquid ordering at the water/MgO(111) interface probed by surface x-ray diffraction"

Conferences

- Physical Electrical Conference (PEC) (June 2010)

  Title: Investigation of $ZnO(000\hat{1})\sqrt{3} \times \sqrt{3}R30$ surface reconstruction
- Argonne National Laboratory User meeting (May 2011)

  Title: Reconstructed structure of water on MgO(111) interface probed by x-ray diffraction
- Argonne National Laboratory User meeting (Sep 2013)

  Tittle: Surface x-ray diffraction study on polar oxide surface/interface